Resource

Cell Reports

BRAF^{V600E} Kinase Domain Duplication Identified in Therapy-Refractory Melanoma Patient-Derived Xenografts

Graphical Abstract

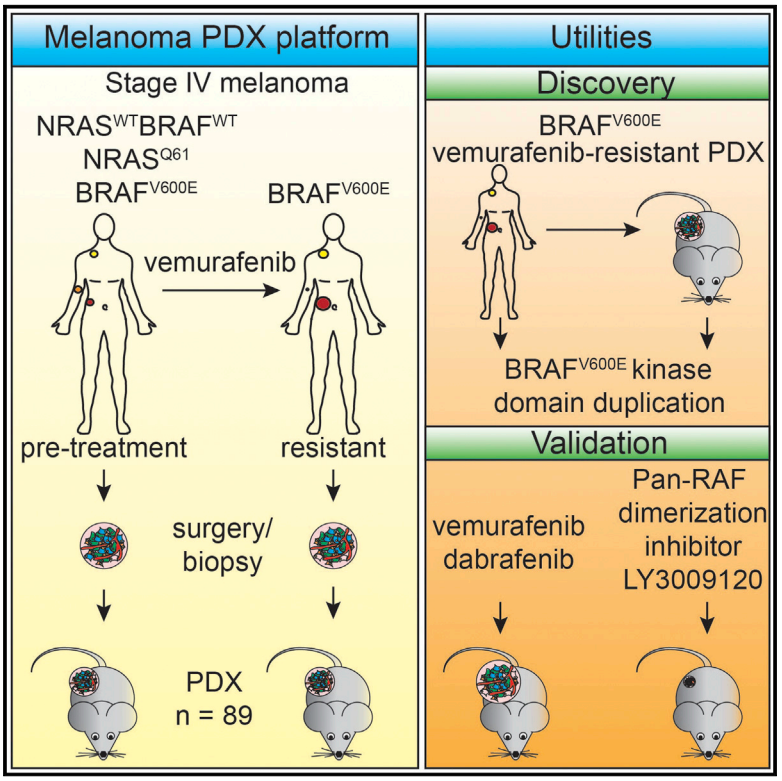

Highlights

- Patient-derived xenograft (PDX) platform comprises 89 metastatic melanoma tumors
- Platform includes several pre-vemurafenib and vemurafenib-resistant PDXs
- Duplication of the BRAF^{V600E} kinase domain is identified as a resistance mechanism
- Pan-RAF dimerization inhibitor LY3009120 eliminates melanoma cells with this duplication

Authors

Kristel Kemper, Oscar Krijgsman, Xiangjun Kong, ..., Christian U. Blank, John B. Haanen, Daniel S. Peeper

Correspondence

d.peeper@nki.nl

In Brief

Kemper et al. have built a platform composed of 89 metastatic melanoma xenografts. Using this collection as a resource, they identified a BRAF^{V600E} protein harboring a duplicated kinase domain. A pan-RAF dimerization inhibitor suppresses expansion of PDXs expressing this BRAF mutant.

Kemper et al., 2016, Cell Reports *16*, 263–277
June 28, 2016
http://dx.doi.org/10.1016/j.celrep.2016.05.064

CellPress

Cell Reports
Resource

$BRAF^{V600E}$ Kinase Domain Duplication Identified in Therapy-Refractory Melanoma Patient-Derived Xenografts

Kristel Kemper,[1,9] Oscar Krijgsman,[1,9] Xiangjun Kong,[1] Paulien Cornelissen-Steijger,[1] Aida Shahrabi,[1] Fleur Weeber,[1] Daphne L. van der Velden,[1] Onno B. Bleijerveld,[2] Thomas Kuilman,[1] Roel J.C. Kluin,[3] Chong Sun,[4] Emile E. Voest,[1] Young Seok Ju,[5] Ton N.M. Schumacher,[6] A.F. Maarten Altelaar,[2,7] Ultan McDermott,[5] David J. Adams,[8] Christian U. Blank,[6] John B. Haanen,[6] and Daniel S. Peeper[1,*]

[1]Division of Molecular Oncology, The Netherlands Cancer Institute, Plesmanlaan 121, 1066 CX Amsterdam, the Netherlands
[2]Mass Spectrometry/Proteomics Facility, The Netherlands Cancer Institute, Plesmanlaan 121, 1066 CX Amsterdam, the Netherlands
[3]Central Genomics Facility, The Netherlands Cancer Institute, Plesmanlaan 121, 1066 CX Amsterdam, the Netherlands
[4]Division of Molecular Carcinogenesis, The Netherlands Cancer Institute, Plesmanlaan 121, 1066 CX Amsterdam, the Netherlands
[5]Cancer Genome Project, The Wellcome Trust Sanger Institute, Hinxton, Cambridge CB10 1SA, UK
[6]Division of Immunology, The Netherlands Cancer Institute, Plesmanlaan 121, 1066 CX Amsterdam, the Netherlands
[7]Biomolecular Mass Spectrometry and Proteomics, Bijvoet Centre for Biomolecular Research and Utrecht Institute for Pharmaceutical Sciences, University of Utrecht, Padualaan 8, 3584 CH Utrecht, the Netherlands
[8]Experimental Cancer Genetics, The Wellcome Trust Sanger Institute, Hinxton, Cambridge CB10 1HH, UK
[9]Co-first author
*Correspondence: d.peeper@nki.nl
http://dx.doi.org/10.1016/j.celrep.2016.05.064

SUMMARY

The therapeutic landscape of melanoma is improving rapidly. Targeted inhibitors show promising results, but drug resistance often limits durable clinical responses. There is a need for in vivo systems that allow for mechanistic drug resistance studies and (combinatorial) treatment optimization. Therefore, we established a large collection of patient-derived xenografts (PDXs), derived from $BRAF^{V600E}$, $NRAS^{Q61}$, or $BRAF^{WT}$/$NRAS^{WT}$ melanoma metastases prior to treatment with BRAF inhibitor and after resistance had occurred. Taking advantage of PDXs as a limitless source, we screened tumor lysates for resistance mechanisms. We identified a $BRAF^{V600E}$ protein harboring a kinase domain duplication ($BRAF^{V600E/DK}$) in ~10% of the cases, both in PDXs and in an independent patient cohort. While $BRAF^{V600E/DK}$ depletion restored sensitivity to BRAF inhibition, a pan-RAF dimerization inhibitor effectively eliminated $BRAF^{V600E/DK}$-expressing cells. These results illustrate the utility of this PDX platform and warrant clinical validation of BRAF dimerization inhibitors for this group of melanoma patients.

INTRODUCTION

Until 5 years ago, treatment options for metastatic melanoma were limited to chemotherapy, which did not significantly improve patient survival. However, the genetic characterization of melanoma (Davies et al., 2002) has prompted the development of therapies targeting specifically the oncogenic drivers of the disease. Approximately half of the patients diagnosed with metastatic melanoma harbor an activating mutation in *BRAF*, most commonly *T1799A*. This encodes the $BRAF^{V600E}$ protein, which renders these patients eligible for treatment with selective BRAF inhibitors. In clinical trials, the first of these inhibitors, vemurafenib, elicited partial or complete tumor regression in the majority of patients (Chapman et al., 2011; Flaherty et al., 2010).

Despite these promising results, while some patients show remarkable durable responses to BRAF inhibition (BRAFi), the majority show an initial response to vemurafenib but eventually develop resistance (Solit and Rosen, 2014). Accounting for this are a plethora of resistance mechanisms, including reactivation of the MAPK pathway, the PI3K/AKT pathway, or both (Nazarian et al., 2010; Paraiso et al., 2011; Poulikakos et al., 2011; Shi et al., 2012, 2014a; Das Thakur et al., 2013; Wagenaar et al., 2014; Wagle et al., 2011). As the majority of resistance mechanisms cause reactivation of the MAPK pathway (Van Allen et al., 2014), a logical next step was to determine the clinical benefit of combinatorial treatment of a MEK inhibitor (e.g., trametinib or cobimetinib) with a BRAF inhibitor (vemurafenib or dabrafenib). The response to such combined treatment was significantly more durable than what was seen for single BRAFi (Larkin et al., 2014; Robert et al., 2015). Still also in the combination treatment setting, resistance again limited overall survival benefit (Hugo et al., 2015; Wagle et al., 2014). Because of these major challenges, there is a dire need to develop more effective (combinatorial) treatment regimens.

Resistance to targeted drugs is mostly studied in in vitro cell models (Basile et al., 2012; Nazarian et al., 2010; Poulikakos et al., 2011; Vergani et al., 2011), but the use of long-term cultured cancer cell lines has several limitations. First, they do

not reliably predict the clinical effect of therapeutics (Burchill, 2006; Voskoglou-Nomikos et al., 2003). Second, the monolayer character of cell culture does not recapitulate the 3D interactions between stromal and cancer cells, which influence not only the dynamics of tumor progression but also therapy response (Straussman et al., 2012). Moreover, the establishment of 2D cell lines from human cancers can induce irreversible changes, including genetic aberrations (De Witt Hamer et al., 2008), alterations in gene expression (Daniel et al., 2009), or dependencies on certain signaling pathways (Clement et al., 2007). Importantly, these properties are not restored upon xenografting of cell lines (Daniel et al., 2009).

A clinically useful model would therefore be to implant tumor fragments derived from patients immediately into mice, thereby cancelling the opportunity for tumors to acquire alterations resulting from in vitro culturing. Such patient-derived xenografts (PDXs) already have been established for several tumor types, including colon cancer (Bertotti et al., 2011), pancreatic cancer (Rubio-Viqueira et al., 2006), breast cancer (DeRose et al., 2011), and melanoma (Einarsdottir et al., 2014; Girotti et al., 2016; Monsma et al., 2015; Das Thakur et al., 2013). Some of these PDX models proved successful in large-scale assessment of the effect of several (combinatorial) therapies and to identify stratification markers, discriminating subgroups of tumors divergently responding to targeted therapy (Bertotti et al., 2011; Gao et al., 2015).

Therefore, we have established a model for metastatic melanoma in which the complex interactions between tumors and at least some components of the tumor microenvironment are maintained. Here we present a collection comprising 89 PDXs established from human metastatic melanomas, which were acquired either before the start of therapy or after the emergence of resistance. This comprehensive PDX platform was analyzed for biomarkers, chromosomal aberrations, RNA expression profiles, mutational spectrum, genetic heterogeneity, and targeted drug resistance patterns. In addition, we tested the utility of this platform as a limitless source of patients' tumor material by screening for resistance mechanisms. Collectively, our results demonstrate that this platform is highly suitable for studying resistance, discovering additional drug targets for companion treatment, and for preclinical studies of human melanoma in general.

RESULTS

Establishment of a PDX Platform for Metastatic Melanoma

Tumor specimens were obtained from patients diagnosed with $BRAF^{V600E}$, $NRAS^{Q61}$, or $BRAF^{WT}NRAS^{WT}$ metastatic melanoma during surgery or by fine-needle biopsy of mainly subcutaneous lesions. Tumor fragments were immediately transplanted subcutaneously into immunodeficient NOD.Cg-*Prkdc*^{scid} *Il2rg*^{tm1Wjl}/SzJ (NSG) mice with a success rate of 86%. This yielded a total of 89 PDXs, comprising 73 $BRAF^{V600E}$, 10 $NRAS^{Q61}$, and 6 $BRAF^{WT}NRAS^{WT}$ xenografts (Table S1). Our attempt to generate cell lines from these PDX samples was successful in 30% of the cases (Table S1). After a first passage in mice (.X1), tumor fragments or digests could be propagated in vivo (.X2, Figure 1A) or cryopreserved for later use. Passaging in mice led to a gradual increase in the tumor outgrowth kinetics (Figure 1B), probably due to loss of human stromal components, consistent with PDXs derived from other tumor types (DeRose et al., 2011; Monsma et al., 2012).

Stable Melanoma Marker Expression, Chromosomal Aberrations, and Gene Expression upon In Vivo Passaging of PDXs

We next determined the effect of passaging PDXs in vivo on melanoma marker expression, chromosomal aberrations, and RNA profiles. First, immunohistochemistry (IHC) for melanoma markers Melan-A, S100, gp-100, and tyrosinase, commonly used for the clinical diagnosis of melanoma, showed that melanoma marker expression remained stable when the patient's tumor was compared to two consecutive passages in vivo as PDXs (Figure 1C; Figure S1).

Second, chromosomal aberrations, analyzed by array comparative genomic hybridization (array CGH), revealed that the genetic heterogeneity was captured in the PDXs (Figures 1D and 1E): passaging of M013 in mice revealed that at least some of the genetic aberrations found in the parental tumor were heterogeneous. For instance, the loss of chromosome 10, which was observed in the patient's tumor, could be detected in one of three first-passage PDXs only, suggesting that chromosome 10 had not been lost in all parental tumor cells (Figure 1D). This is consistent with recent studies by us and others showing that melanomas are highly heterogeneous (Kemper et al., 2015; Shi et al., 2014b; Van Allen et al., 2014). Also passaging of M003 in mice revealed a variable pattern, which can be explained either by heterogeneity in the original tumor or by loss of genomic variation upon in vivo passaging. Importantly, after the first passage, the chromosomal content was stable and highly similar to the parental chromosomal content (Figure 1E).

Third, we analyzed gene expression patterns, comparing patient samples to their corresponding PDXs. We obtained samples for PDX establishment from four different patients, with tumor samples taken either before the start of vemurafenib treatment or after a patient had acquired therapy resistance (indicated by R). RNA was isolated from both patients' tumors and PDXs and gene expression profiling was done by RNA sequencing. Hierarchical clustering of all samples was performed, resulting in a clustering that revealed a high concordance in gene expression between the patient samples and their corresponding PDXs (Figure 1F).

Together, these data show that, during the passaging of human melanomas in mice, the phenotypic and genetic characteristics are well preserved, yielding a collection of PDXs closely resembling the original patients' tumors.

Clinical History of Patients from Matched Pre- and Post-vemurafenib PDX Pairs

We acquired a set of six matched PDX pairs, representing tumor material from patients both before the start of treatment with vemurafenib and after resistance had occurred (indicated by R). We illustrated the treatment schedule, the location of the lesion from where material was obtained for xenografting, and the

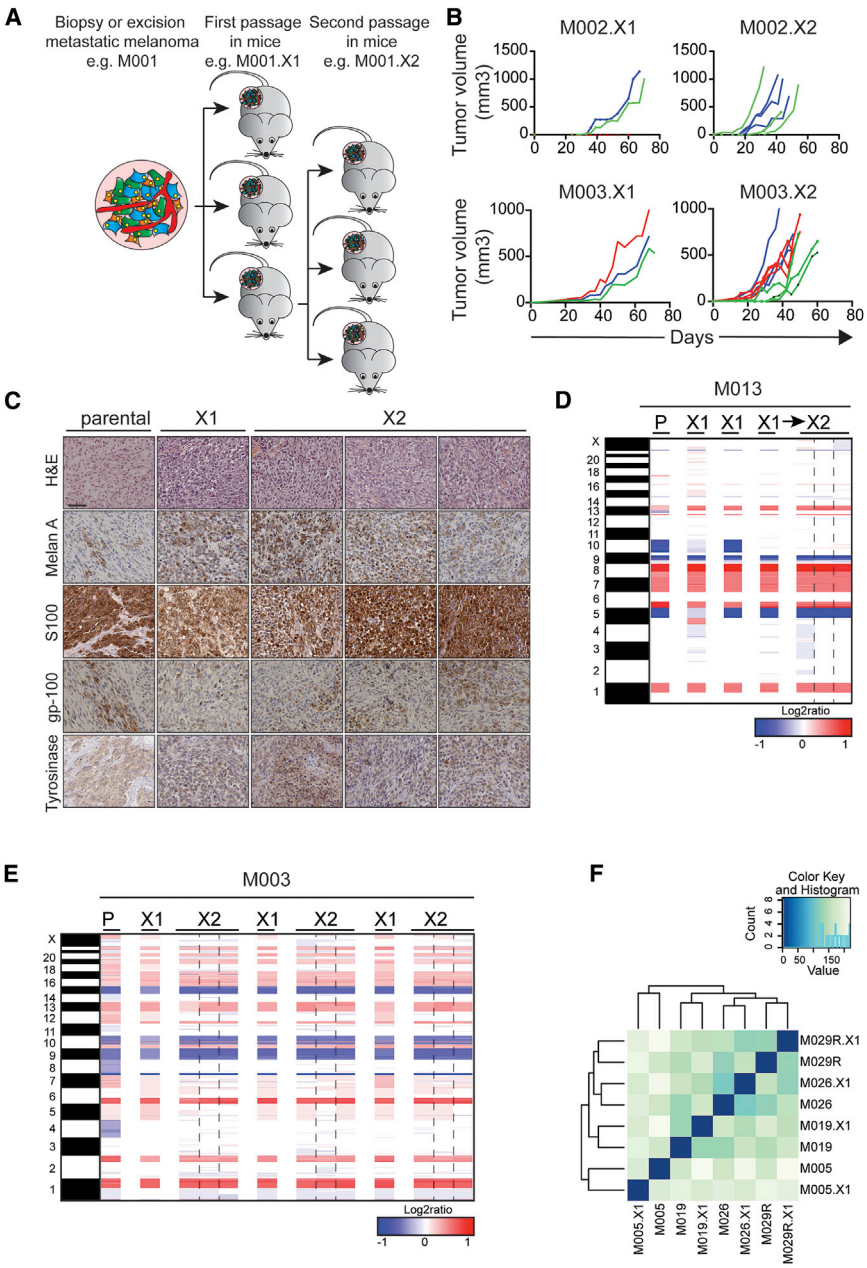

Figure 1. Stable Melanoma Marker Expression, Chromosomal Aberrations, and Gene Expression upon In Vivo Passaging of PDXs

(A) Tumor fragments derived from biopsies or surgical excisions were transplanted subcutaneously into NSG mice. After first passage (.X1), PDX fragments were passaged into a next set of mice (.X2).

(B) Speed of tumor outgrowth during passaging, shown for two different PDXs. Colors represent single PDX (.X1) passaged into a next set of three mice (.X2).

(C) H&E stainings and IHC stainings for MelanA, S100, gp-100, and tyrosinase were performed on the parental tumor and two subsequent passages of PDXs (X1 and X2). Scale bars indicate 100 μm.

(D) Copy-number profiles, based on array CGH, show the parental tumor (P) M013 and two PDX passages (the X2 passage was established from the third X1 PDX).

(E) Copy-number profiles, based on array CGH, show the parental tumor (P) M003 and two PDX passages (the X2 passages are next to their own X1-passaged PDX). Blue, deletion; red, amplification.

(F) Hierarchical clustering of RNA-sequencing data performed on patient samples and PDXs derived of these samples, after filtering as described in the Supplemental Experimental Procedures, is shown.

specific response of these lesions to vemurafenib in Figure S2. In four patients, the resistant lesions, from which post-treatment PDXs were derived, either initially responded to vemurafenib before acquiring resistance (M009R, M026R, and M048R1; Figure S2) or emerged as new lesions during treatment (M029R and M048R2; Figure S2). Therefore, this group of PDXs was labeled acquired resistant. One matched pair (M005) was derived from a patient who was still responding to vemurafenib when the post-treatment sample was obtained, and was therefore categorized as on treatment. The sixth PDX pair was acquired from a patient (M019) who progressed immediately on vemurafenib treatment, qualifying these melanomas as intrinsic resistant (Figure S2).

Vemurafenib-Resistant PDXs Commonly Display MAPK Pathway Reactivation

Several groups, including ours, have demonstrated that the MAPK pathway and, to a lesser extent, the PI3K pathway are commonly reactivated in vemurafenib-resistant melanomas (Kemper et al., 2015; Shi et al., 2014b; Van Allen et al., 2014). To determine whether this was recapitulated in our matched PDX series, we performed immunoblotting for phosphorylated ERK (p-ERK) and AKT (p-AKT). Indeed, all four acquired resistant PDXs from the matched pair set had reactivated p-ERK (Figure 2A), which was confirmed by IHC (Figure S3A). Only one PDX pair, namely M048, also showed reactivated p-AKT (Figure 2A). As expected, the PDX of the intrinsically resistant patient M019 already showed elevated p-ERK and p-AKT levels in the pre-treatment setting, while p-ERK was relatively low in the PDX from the on-treatment patient (Figure 2A; Figure S3A).

Previously, we and others have shown that acquired resistance to BRAFi is effectively brought about by the loss of expression of microphthalmia-associated transcription factor (MITF) (Konieczkowski et al., 2014; Müller et al., 2014). Consistent with this, we observed decreased expression of MITF in three acquired resistant post-vemurafenib PDXs

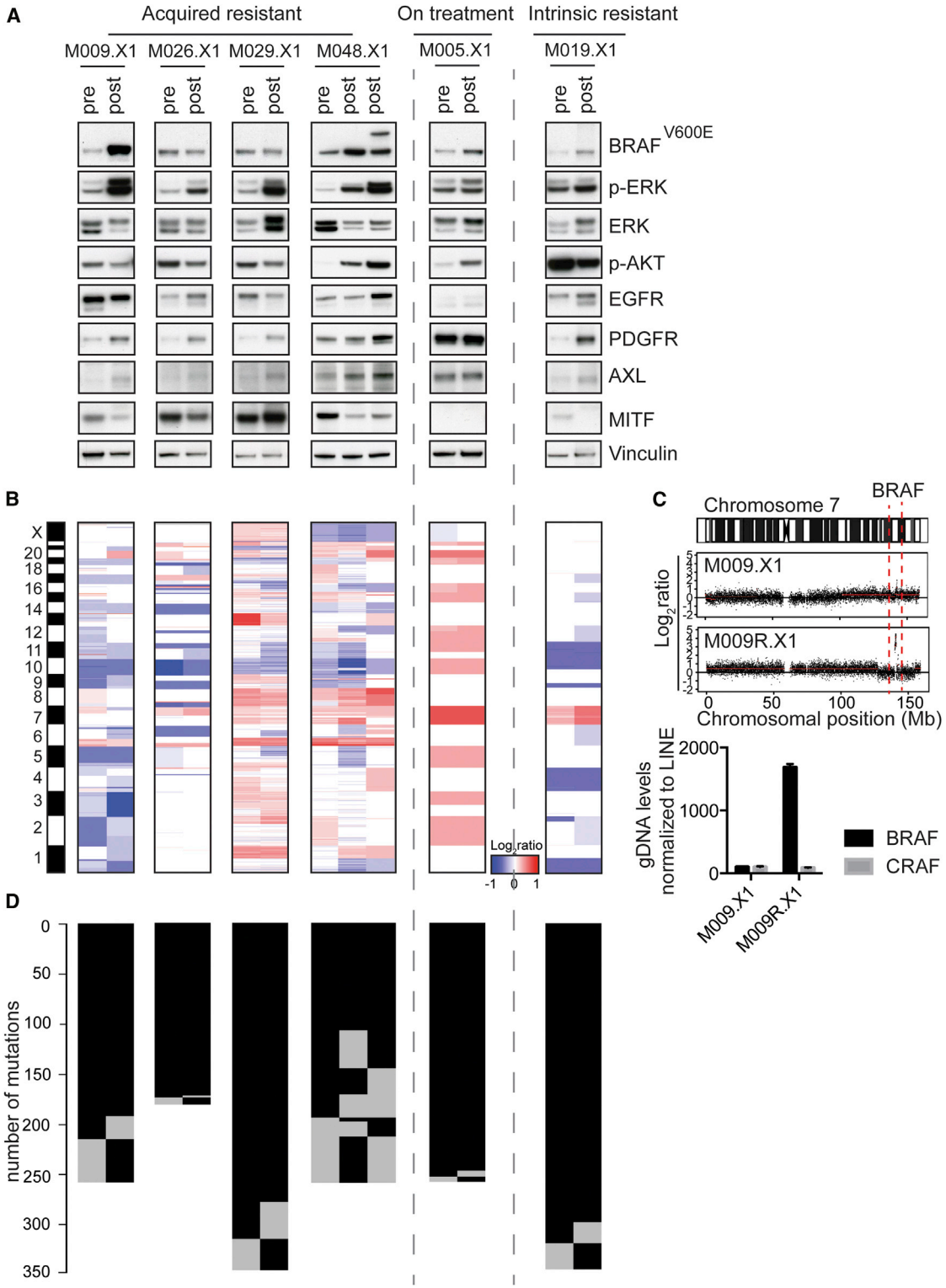

Figure 2. Vemurafenib-Resistant PDXs Commonly Display MAPK Pathway Reactivation and Have Distinct Resistance Mechanisms

(A) Immunoblotting of all six matched PDX pairs for factors in the MAPK pathway in pre-vemurafenib and post-relapse PDXs. Asterisks indicate PDXs that were xenografted in mice that received PLX4720 chow.

(B) Copy-number profiles for matched PDX pairs, determined by CopywriteR, are shown.

(legend continued on next page)

(M009R.X1, M026R.X1, and M048R.X1; Figure 2A). Reduced expression of MITF coincides with upregulation of one or multiple receptor tyrosine kinases (RTKs), such as EGFR, PDGFR, and, most commonly, AXL (Konieczkowski et al., 2014; Müller et al., 2014), which was well recapitulated in these matched acquired resistant PDXs (Figure 2A). Only M029R.X1 displayed increased expression of MITF expression upon acquired resistance (Figure 2A), which also previously has been reported as a resistance mechanism to MAPK pathway inhibition (Garraway et al., 2005; Müller et al., 2014).

In conclusion, our series of matched PDXs captures the resistance biomarkers that are commonly seen in drug-resistant melanomas in patients.

Identification of Resistance Mechanisms in Matched PDX Pairs

To uncover the cause of resistance in the matched PDX pairs, we performed whole-exome sequencing (WES) on genomic DNA (gDNA) derived from all matched PDXs. The level of tumor infiltration by mouse stroma was determined by a mouse pathologist via analysis of formalin-fixed paraffin-embedded (FFPE) H&E stainings of these PDXs, revealing that most PDXs contained >80% of tumor cells (Table S2). XenofilteR (R.J.C.K. and O.K., unpublished data) was used to remove all sequence reads that originated from mouse DNA. Copy-number profiles were generated from the filtered WES data by CopywriteR (Kuilman et al., 2015) (Figure 2B). This analysis revealed that pre- and post-vemurafenib PDXs had highly similar DNA copy-number profiles, although some variation was observed. This could result from inter-tumor heterogeneity, as most pre- and post-vemurafenib PDXs were not derived from the same patient lesion (Figure S2B). When analyzing copy-number aberrations (CNAs) in more detail, we detected a $BRAF^{T1799A}$ amplification, an established resistance mechanism (Shi et al., 2014b; Das Thakur et al., 2013; Van Allen et al., 2014), in the resistant M009R.X1, but not in the pre-treatment PDX (Figure 2C, top panel). This amplification was validated by qPCR on gDNA (Figure 2C, bottom panel). None of the other resistant PDXs displayed an amplification of $BRAF^{T1799A}$ (Figures S3B and S3C).

Next we analyzed the presence of mutations in the matched PDX pairs (Figure 2D). The BRAFi resistance-inducing mutation $NRAS^{Q61K}$ (Nazarian et al., 2010) was detected in two of the post-vemurafenib PDXs (M026R.X1 and M029R.X1) and was confirmed by Sanger sequencing (Figures S4A and S4B). In M048R2.X1, a mutation in AKT3 (L51R) (Catalogue of Somatic Mutations in Cancer [COSMIC]: COSM309035) was detected and confirmed by Sanger sequencing (Figure S4C). This mutation has not been validated yet as a cause of resistance, but two other previously described resistance-conferring mutations, namely $AKT3^{E17K}$ and $AKT1^{Q79K}$ (Shi et al., 2014a, 2014b), are located within the same pleckstrin homology (PH) domain as $AKT3^{L51R}$. These mutations induce (re)localization of AKT to the membrane, causing constitutive activation of the PI3K/AKT pathway (Parikh et al., 2012). The M048R2.X1 PDX, harboring this $AKT3^{L51R}$ mutation, indeed displays highly activated AKT (Figure 2A), suggesting that this mutation activates the kinase activity.

In summary, we have identified $BRAF^{T1799A}$ amplification and $NRAS^{Q61K}$ and $AKT3^{L51R}$ mutations as the likely causes for vemurafenib resistance in our matched acquired resistant PDX pairs, capturing the mutational spectrum seen in resistant human melanomas.

Validation of Resistance to BRAFi In Vivo in Matched PDX Pairs

The next step was to confirm that PDXs derived from vemurafenib-naive $BRAF^{V600E}$ lesions were responsive to BRAFi in vivo, in contrast to PDXs from vemurafenib-resistant melanomas. We first analyzed the response to the BRAFi dabrafenib of the matched M026 PDX pair. The treatment-naive M026.X2 melanoma was highly sensitive to BRAFi, resulting in reduced growth and a decrease in p-ERK abundance upon BRAFi (Figures 3A and 3B; Figure S4D). In contrast, M026R.X2, a PDX derived from a vemurafenib-resistant lesion from the same patient in which we identified a $NRAS^{Q61K}$ mutation as the resistance mechanism (Figures S4A and S4B), was completely resistant to BRAFi (Figure 3A). Consistently, p-ERK levels of M026R.X2 were unaffected by BRAFi (Figure 3B). A similar pattern was observed for the matched M029 PDX pair: treatment-naive melanoma M029.X2 responded well to BRAFi along with p-ERK inhibition, whereas tumor outgrowth of $NRAS^{Q61K}$ mutant M029R.X2 and its p-ERK levels were unaffected by BRAFi (Figures 3A and 3B; Figure S4D). Of note, the growth rate of the (untreated) M029R.X2 was much slower than that of its treatment-naive counterpart M029.X2.

This behavior was different for matched pair M009.X2/R.X2, in which the presence of the $BRAF^{T1799A}$ amplification correlated with therapy resistance. For this PDX set, expansion of the treatment-naive M009.X2 melanoma was reduced upon BRAFi and p-ERK levels decreased, as expected (Figures 3A and 3B; Figure S4D). However, BRAFi also slowed down the growth and decreased p-ERK levels of M009R.X2, which was derived from a vemurafenib-resistant lesion (Figures 3A and 3B; Figure S4D). This coincided with two interesting observations. First, M009R.X2 grew much faster than M009.X2. Therefore, in spite of the notable effect of BRAFi, M009R.X2 continued to grow exponentially. Second, expression of $BRAF^{V600E}$, although already highly expressed in M009R.X2 when compared to M009.X2, was even further increased upon BRAFi (Figures 3C and 3D). The cause for this is unknown but could reflect either a dosage change in the $BRAF^{T1799A}$ gene or selection for a subpopulation

(C) Amplification of the genomic region containing $BRAF^{T1799A}$ was identified in M009R.X1 (top panel). Validation of this amplification was performed by qPCR on gDNA (bottom panel). *CRAF* was included as a negative control. CT values were normalized to *LINE*.
(D) Mutation matrix for matched PDX pairs, comparing pre-vemurafenib and post-relapse tumors. Number of mutations is indicated; each black line represents one mutation.

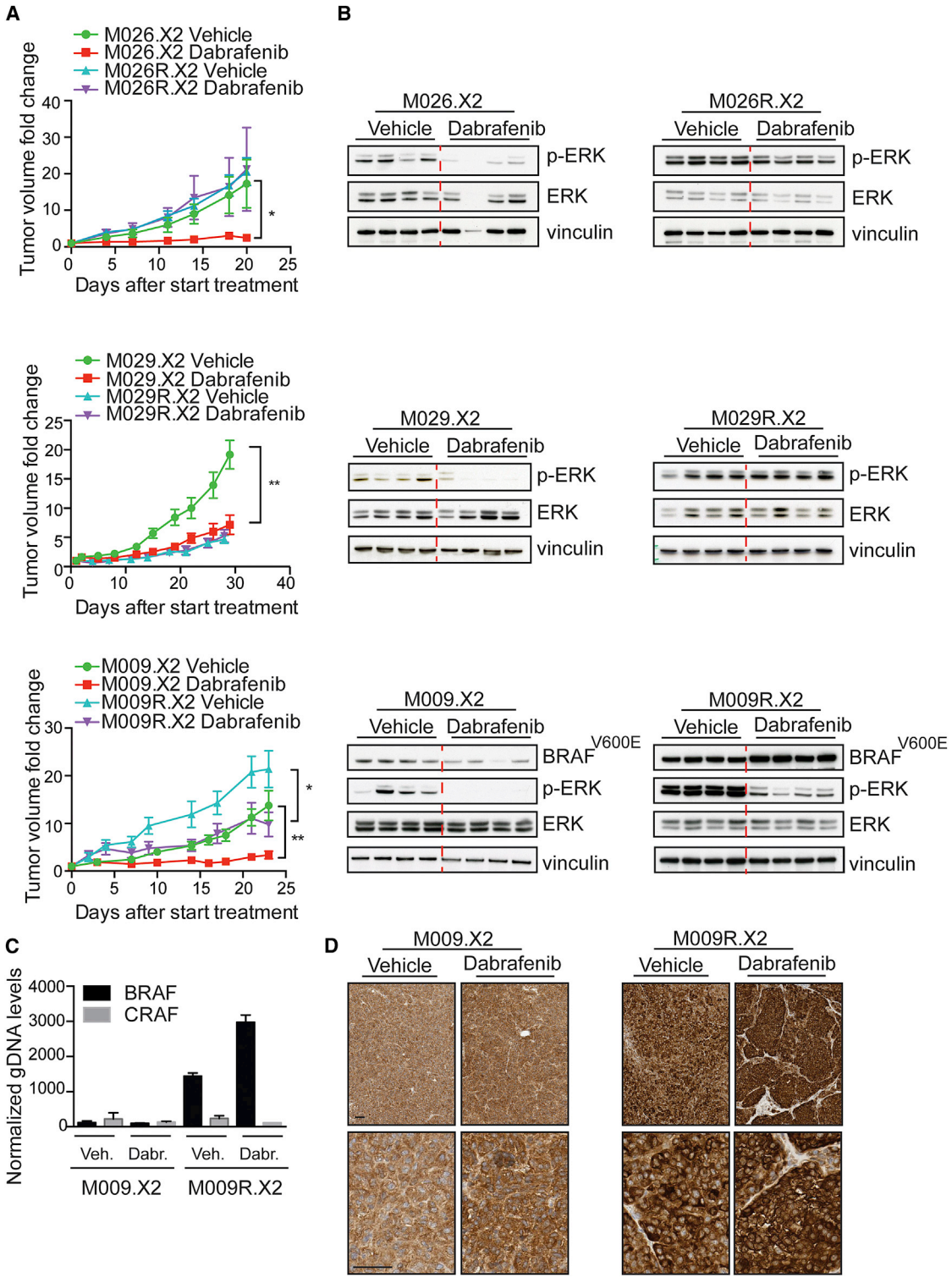

Figure 3. Validation of Resistance to BRAFi In Vivo in Matched PDX Pairs

(A) Tumor dynamics of matched PDX pairs upon treatment with 30 mg/kg dabrafenib (n = 8 tumors/group). Graphs represent fold change in tumor volume relative to the tumor volume at treatment initiation. Unpaired t test was performed at the last time point (*p < 0.05 and **p < 0.01). Error bars indicate SD.

(legend continued on next page)

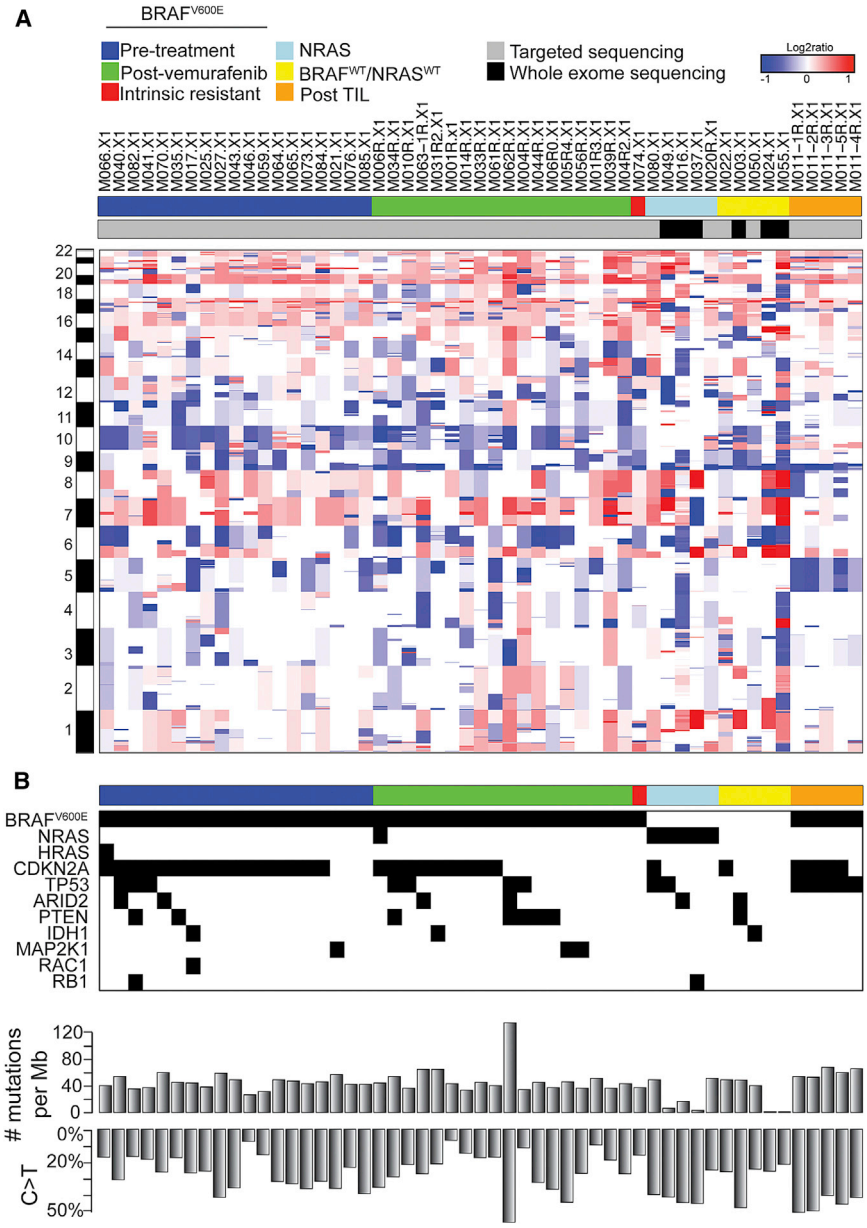

Figure 4. Mutational Characterization of the PDX Panel

(A) Targeted sequencing for 360 cancer genes was performed on 47 PDXs, and WES was performed on an additional six PDXs. Copy number profiles were derived from these data. PDXs were grouped in pre-BRAF inhibitor treatment (pre-treatment), BRAF inhibitor-resistant (post-vemurafenib), intrinsic resistant, $NRAS^{Q61}$ mutant (NRAS), and $BRAF^{WT}NRAS^{WT}$ PDXs and PDXs derived from five different lesions for a single patient after tumor-infiltrating lymphocytes therapy (post-TIL).

(B) Mutation matrix for 11 known melanoma driver genes. Total number of mutations per 1 Mb and the percentage of mutations with a C > T are indicated below the mutation matrix.

Mutational Characterization of the PDX Panel

In addition to six matched PDX pairs, the collection comprises an additional 76 melanoma PDXs. Targeted sequencing using a 360-cancer gene panel was performed for more than half of these. The 47 PDXs comprise the following: (1) $BRAF^{V600E}$ PDXs derived from vemurafenib-naive or -resistant melanomas, (2) $NRAS^{Q61}$ PDXs, (3) $BRAF^{WT}/NRAS^{WT}$ PDXs, and (4) a set of five PDXs derived from different lesions of one patient who received tumor-infiltrating lymphocyte (TIL) therapy. Additionally, for six PDXs, comprising three $NRAS^{Q61}$ and three $BRAF^{WT}NRAS^{WT}$ PDXs, WES was performed.

Using CopywriteR, we generated copy-number profiles from the sequencing data (Figure 4A). These profiles revealed a CNA pattern typical of melanoma, including gain of chromosome 7, where *BRAF* is located, and loss of chromosome 10, which harbors the tumor suppressor gene *PTEN*, both established drivers of melanomagenesis. Next we analyzed which mutations are present in our PDX panel, focusing on mutations in the 15 driver genes on which the molecular classification of melanomas has been described previously (Cancer Genome Atlas Network, 2015) (Figure 4B). For 11 of 15 driver genes, mutations were observed in the 53 PDX samples. The complete list of mutations identified by targeted sequencing is provided in Table S3.

with super-amplification of $BRAF^{T1799A}$. Additionally, this would suggest that the BRAF amplification and the resulting resistance can be dynamic, as has been suggested by others (Das Thakur et al., 2013).

These results demonstrate concordance between drug responses in patients and their corresponding PDXs, and they illustrate that the therapy response can be either stable or dynamic.

(B) Immunoblotting for p-ERK on matched PDX pairs, treated with and without dabrafenib (each lane represents a tumor derived from an individual mouse), is shown.

(C) The $BRAF^{T1799A}$ amplification was validated by qPCR on gDNA. *CRAF* was included as a negative control. CT values were normalized to *LINE*. Error bars indicate SD.

(D) Stainings for $BRAF^{V600E}$ on M009.X2 and M009R.X2, treated with and without BRAF inhibitor. Scale bars indicate 100 μm.

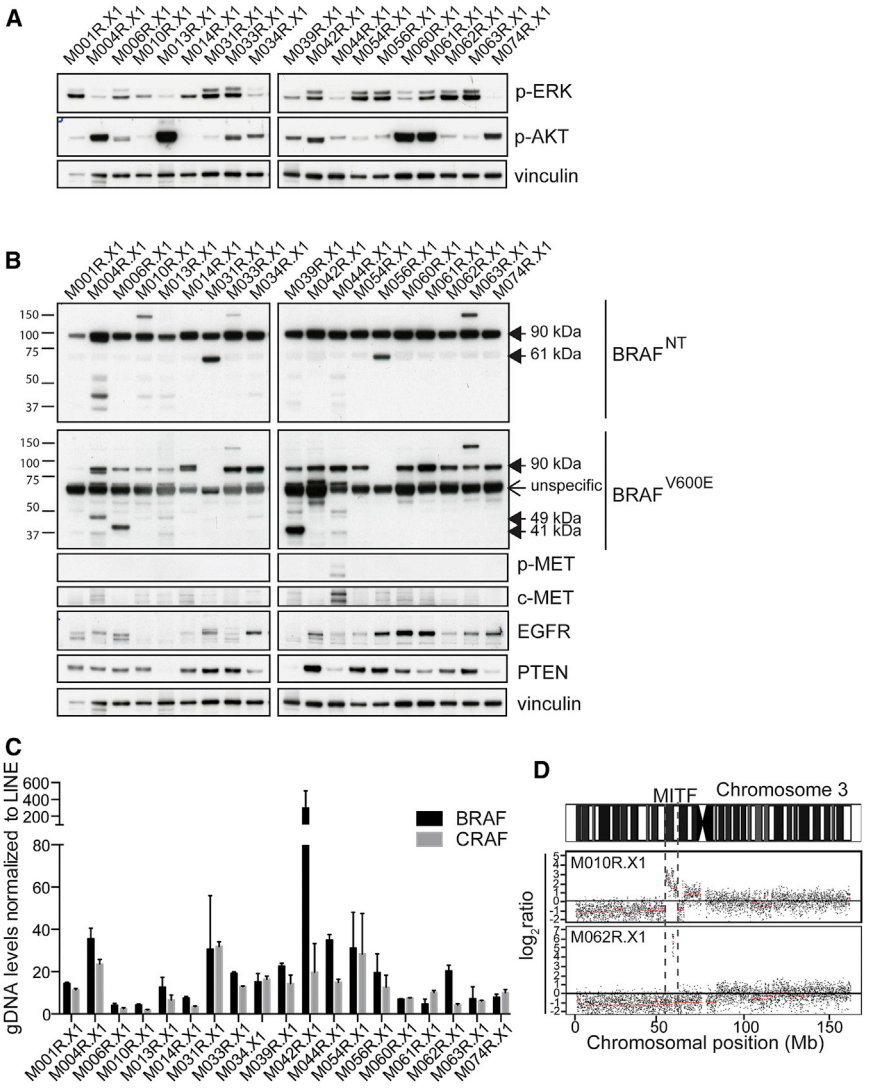

Figure 5. PDXs Derived from Vemurafenib-Resistant Melanomas Harbor a Plethora of Established Clinical Resistance Mechanisms

(A) Immunoblotting for p-ERK and p-AKT to detect reactivation of the MAPK pathway and/or the PI3K/AKT pathway in the post-vemurafenib PDXs. Vinculin was used as a loading control.

(B) Immunoblotting to detect previously described resistance mechanisms in post-vemurafenib PDXs. Vinculin was used as a loading control.

(C) Analysis of *BRAF*^{T1799A} amplification by qPCR on gDNA of all post-vemurafenib PDXs is shown.

(D) DNA copy-number profiles revealed amplification of the region containing *MITF* in two independent PDXs.

PDXs Derived from Vemurafenib-Resistant Melanomas Harbor a Plethora of Established Clinical Resistance Mechanisms

In the panel of 53 sequenced PDXs (Table S4), 19 were derived from BRAF^{V600E} metastatic melanomas that had acquired resistance to vemurafenib. We analyzed this PDX set for the presence of known resistance mechanisms. As discussed above, resistance to vemurafenib is commonly associated with reactivation of the MAPK pathway and/or the PI3K/AKT pathway. Concordantly, when we determined the corresponding biomarker levels in these PDXs, we found that, in most, either p-ERK or p-AKT was highly induced (Figure 5A; Figure S5A).

Next we analyzed BRAF expression by immunoblotting to detect alternative splice variants, which also are known to render melanomas refractory to BRAFi. These variants splice out the RAS-binding domain (RBD) of BRAF (encoded by exons 3–5), inducing dimerization of BRAF and downstream signaling without the need to be activated by RAS (Poulikakos et al., 2011). Several splice variants have been described to induce resistance, i.e., 61-kDa (exons 4–10), 48-kDa (exons 2–8), and 41-kDa (exons 2–10) variants (Poulikakos et al., 2011). Using two different antibodies, recognizing either the N-terminal (BRAF^{NT}, epitope encoded by exons 2–3) or the V600E region (BRAF^{V600E}, epitope in exon 15), we detected these different splice variants in several PDXs (Figure 5B).

We also identified other previously detected and validated resistance mechanisms in the post-vemurafenib PDX panel, including hyperactivation of c-MET (Vergani et al., 2011), EGFR overexpression (Sun et al., 2014), loss of PTEN (Paraiso et al., 2011) (Figure 5B), amplification of *BRAF*^{T1799A} (Shi et al., 2014b) (Figure 5C), and amplification of *MITF* (Garraway et al., 2005; Van Allen et al., 2014) (Figure 5D). Additionally, using the targeted sequencing data, we found known BRAF inhibitor resistance-conferring mutations, including MAP2K1^{E203K} (Nikolaev et al., 2011), BRAF^{L505H} (Wagenaar et al., 2014), NRAS^{Q61K} (Nazarian et al., 2010), and PIK3CA^{E545K} (Shi et al., 2014b) (Table S5).

Through a combination of mutational data with biochemical analyses, the cause of resistance was resolved for 13 of the 19 PDXs derived from patients with acquired resistance to vemurafenib. This also revealed that some PDXs harbor multiple resistance mechanisms (Table S5). For example, M056R.X1 harbored a MAP2K1^{E203K} mutation, alternative BRAF splicing, as well as EGFR overexpression, indicating that resistance mechanisms can be heterogeneous (Kemper et al., 2015; Shi et al., 2014b). Our data show that this heterogeneity is captured and maintained in PDXs.

To summarize, this set of post-vemurafenib PDXs harbors a wide range of resistance mechanisms, closely recapitulating clinical samples. Some PDXs harbored multiple resistance mechanisms, a phenomenon commonly seen in melanoma,

indicating that the heterogeneity of resistance can be maintained in these PDX models.

PDXs Derived from Vemurafenib-Resistant Patients Express a BRAF^{V600E} Mutant Harboring a Kinase Domain Duplication

Despite the advances made in targeted therapies for BRAF^{V600E} melanoma, drug resistance continues to be a major obstacle for achieving durable clinical responses. To illustrate the utility of this PDX platform, we set out to screen for resistance mechanisms. We focused on those that can be discovered at the protein level, in other words, using analyses requiring substantial amounts of melanoma tumor material. Thus, we took advantage of our PDX collection serving as an unlimited source for this purpose.

In addition to the previously identified resistance mechanisms described above, we noted that several PDXs derived from vemurafenib-resistant melanomas expressed an unusual BRAF^{V600E} protein, which migrated in an SDS-PAGE gel at an apparent molecular weight of ~140 kDa. It was recognized by both the BRAF^{V600E}- and the BRAF^{NT}-specific antibodies (Figure 2A, M048R2.X1; Figure 5B, M010R.X1, M033R.X1, and M063R.X1). Strikingly, none of the pre-treatment PDXs showed expression of this abnormal BRAF^{V600E} protein (Figure S5B). Furthermore, we discovered similar BRAF proteins in two cell lines that had acquired resistance to MAPK pathway inhibition in vitro (PLX4720-resistant A375R and dabrafenib/trametinib double-resistant [DR] 888mel) (Figure 6A). Importantly, this abnormal BRAF^{V600E} protein also was detected in corresponding patients samples of the PDXs expressing this ~140-kDa BRAF^{V600E} protein (Figure 6B), excluding that this was due to an in vitro or PDX artifact.

To unmask the identity of this apparently common ~140-kDa BRAF^{V600E} protein, we performed whole-genome sequencing (WGS). We observed that resistant melanoma cells harbored genomic rearrangements and partial duplication of the *BRAF* genomic locus: the first breakpoint was located in the intron between exons 9 and 10 of *BRAF^{T1799A}*, while the second breakpoint had occurred in the intron between exons 18 and 19. The resulting duplication contained exons 10–18 of the *BRAF^{T1799A}* gene, which harbors the kinase domain (Figure 6C; Figures S6A–S6F). This was confirmed by PCR using primers specifically for each breakpoint (Figure 6D). We also observed a larger amplification on chromosome 7 of 888melDR, raising the possibility that the locus containing *BRAF^{T1799A}* with the kinase domain duplication was amplified specifically during resistance acquisition (Figures 6E and 6F; Figures S6C and S6D).

To confirm that the duplication of the *BRAF^{T1799A}* kinase domain-encoding region results in the production of a BRAF^{V600E} protein harboring a duplication of its kinase domain (hereafter BRAF$^{V600E/DK}$), we performed RNA sequencing on the four PDXs that expressed the ~140-kDa protein. This revealed that, in three of the four cases, the fusion between exon 18 and exon 10 had occurred at 18 bp 5′ to the stop codon in exon 18 and at the start at exon 10 (Figure 6G). This location in exon 18 recently was identified as a splice donor site (Figure 6G), which is used by melanoma cells to splice to an alternative X1 3′ UTR localized in exon 19 (Marranci et al., 2015). Melanoma cells can thus express BRAF with a normal 3′ UTR (BRAF-N) or with an alternative X1 3′ UTR (BRAF-X1, Figure 6G).

This raised the possibility that, resulting from the genomic rearrangement, the BRAF$^{V600E/DK}$-expressing tumors use this alternative splice donor site in exon 18 to splice to the next exon 10. We validated this predicted fusion on mRNA by RT-PCR, using a forward primer in exon 18 and a reverse primer in exon 10 (Figure 6H). This confirmed the presence of BRAF$^{V600E/DK}$ in three PDXs (M033R.X1, M063R.X1, and M048R2.X1) that showed the ~140-kDa band on immunoblotting (Figure 6A), as well as in two vemurafenib-resistant cell lines (A375R and 888melDR). Also, we confirmed the location of the fusion by Sanger sequencing (Figure 6I). Furthermore, using RNA-sequencing data of an independent set of MAPK pathway inhibition- resistant melanomas (Hugo et al., 2015), we identified the BRAF$^{V600E/DK}$ in four of 44 resistant tumors (Table S6), in which no other genomic mechanism was found to explain the acquired resistance.

To validate the identity and configuration of BRAF$^{V600E/DK}$ independently at the protein level, we performed immunoprecipitation (IP) for BRAF on the 888melDR cell line, which showed very high expression of the endogenous BRAF$^{V600E/DK}$ protein. The samples were run on an SDS-PAGE gel from which the 140-kDa band was excised and subjected to mass spectrometry. The result confirmed the findings from the genetic analyses (Figure S7). Taken together, our data indicate that the genomic breakpoint can occur anywhere between exons 18 and 19 and that the tumors use an alternative splice donor site within exon 18 to splice to the next exon (which is exon 10 in the case of the BRAF$^{V600E/DK}$). This configuration allows for the natural stop codon in exon 18 to remain intact, as it is removed by splicing, resulting in an in-frame kinase domain duplication.

BRAF$^{V600E/DK}$ Is Responsible for Resistance to BRAFi

This is a hitherto unidentified mechanism that may cause resistance to BRAFi. Therefore, we examined whether specific depletion of BRAF$^{V600E/DK}$, but not BRAF^{V600E}, would result in restoration of BRAF inhibitor sensitivity. We designed small hairpin RNAs (shRNAs) specifically targeting the region between exons 18 and 10 in the BRAF$^{V600E/DK}$-encoding mRNA. As expected, these shRNAs depleted the BRAF$^{V600E/DK}$ protein from the A375R or M063R.X1 cells, but not the BRAF^{V600E} protein (Figures 7A and 7B). Only when BRAF$^{V600E/DK}$ was silenced was BRAFi capable of decreasing p-ERK levels. Functional validation of this observation in a colony formation assay revealed that BRAF$^{V600E/DK}$ depletion increased sensitivity to BRAFi, in a dose-dependent manner. These results indicate that specific knockdown of BRAF$^{V600E/DK}$ sensitizes tumor cells to BRAFi (Figures 7C and 7D).

To determine whether BRAF$^{V600E/DK}$ hyperactivates ERK, we overexpressed its cDNA in HEK293T cells. As expected, this resulted in the expression of a 140-kDa protein, which co-migrated with the BRAF$^{V600E/DK}$ protein seen in resistant PDXs and cell lines (Figures 6A and 7E). Indeed, BRAF$^{V600E/DK}$ expression resulted in hyperactivation of ERK (Figure 7E). In agreement with the idea that BRAF$^{V600E/DK}$ constitutively fuels the MAPK pathway even in the presence of BRAF inhibitor, we observed that, upon exposure to vemurafenib, BRAF$^{V600E/DK}$-expressing cells maintained higher levels of active ERK than cells producing BRAF^{V600E} (Figure 7E).

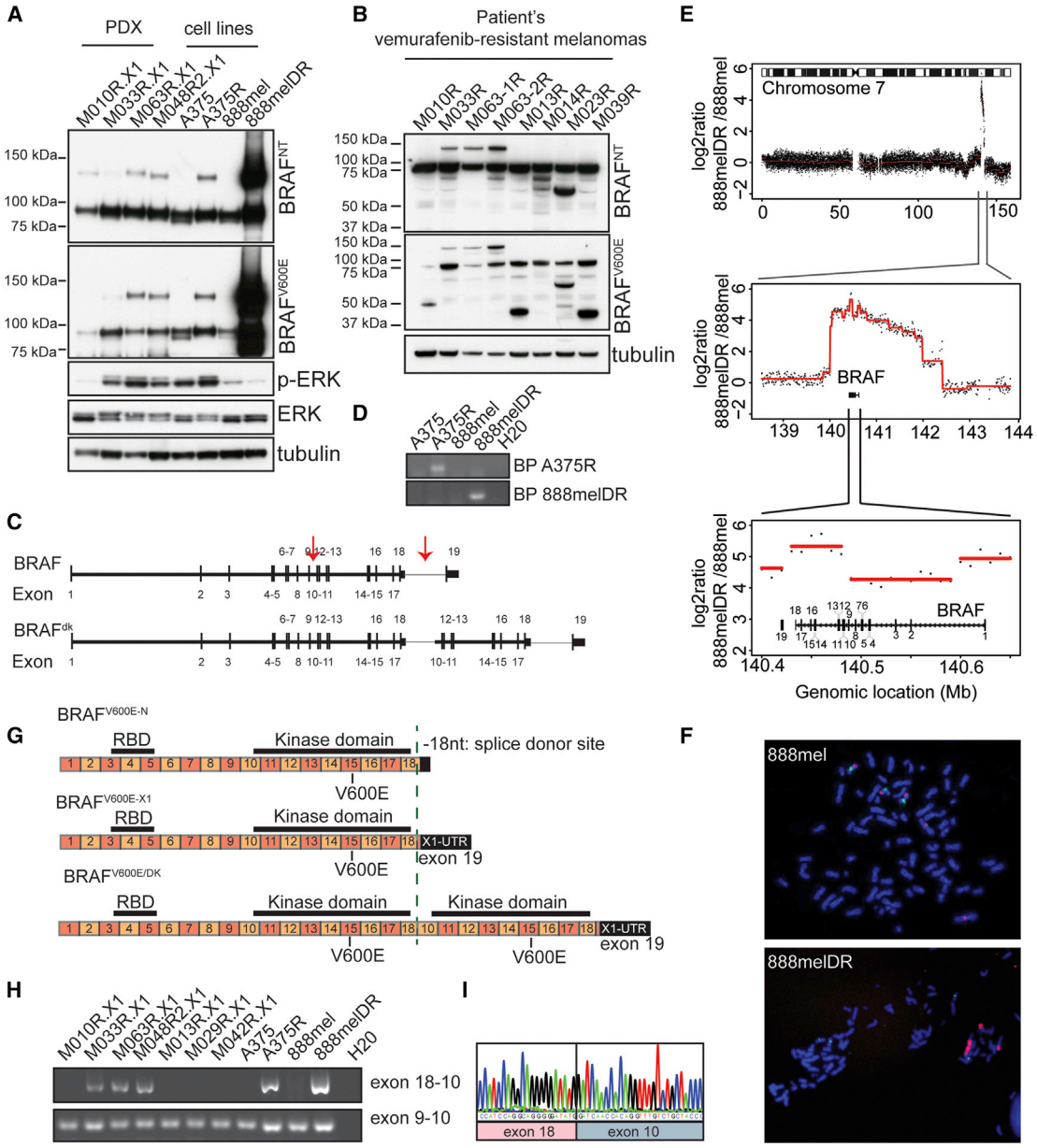

Figure 6. Resistance Mechanism to BRAFi Involving Duplication of the Kinase Domain of BRAF^{V600E} Discovered in PDX Panel

(A) Immunoblotting for BRAF using a set of four PDXs and two in vitro generated melanoma cell lines resistant for PLX4720 (A375R) or dabrafenib/trametinib (888melDR). Tubulin is used as a loading control. BRAF^{NT}, antibody recognizing an epitope encoded by exons 2–3 of *BRAF*; BRAF^{V600E}, antibody recognizing specifically the BRAF^{V600E} epitope.

(B) Immunoblotting for BRAF on patient samples of vemurafenib-resistant lesions is shown.

(C) Representation of BRAF^{V600E} and BRAF$^{V600E/DK}$ at the genomic level. Arrows indicate the introns where the breakpoints are localized. Black vertical bars, exons; horizontal bars, introns.

(D) Validation of specific genomic breakpoints is shown.

(E) DNA copy-number alterations in the 888melDR relative to 888mel cell line for chromosome 7, with magnification of the amplified region and further magnification of the *BRAF* locus, are shown.

(F) Fluorescence in situ hybridization (FISH) of 888mel and 888melDR cell line, using either a BRAF probe (red) or a chromosome 7 centromere probe (green), is shown.

(G) Illustration of BRAF^{V600E}- and BRAF$^{V600E/DK}$-encoding mRNA. Upper row indicates BRAF^{V600E} with normal 3′ UTR (BRAF$^{V600E-N}$), middle row indicates BRAF^{V600E} with alternative X1 3′ UTR (BRAF$^{V600E-X1}$), and bottom row indicates BRAF$^{V600E/DK}$. Green dashed line indicates splice donor site localized within exon 18, which can be used for alternative 3′ UTR splicing.

(H) PCR product using a forward primer in exon 18 and a reverse primer in exon 10 validates the presence of BRAF$^{V600E/DK}$. As a control, primers in exon 9 (forward) and exon 10 (reverse) were used.

(I) Sanger sequencing of PCR product obtained in (H) is shown.

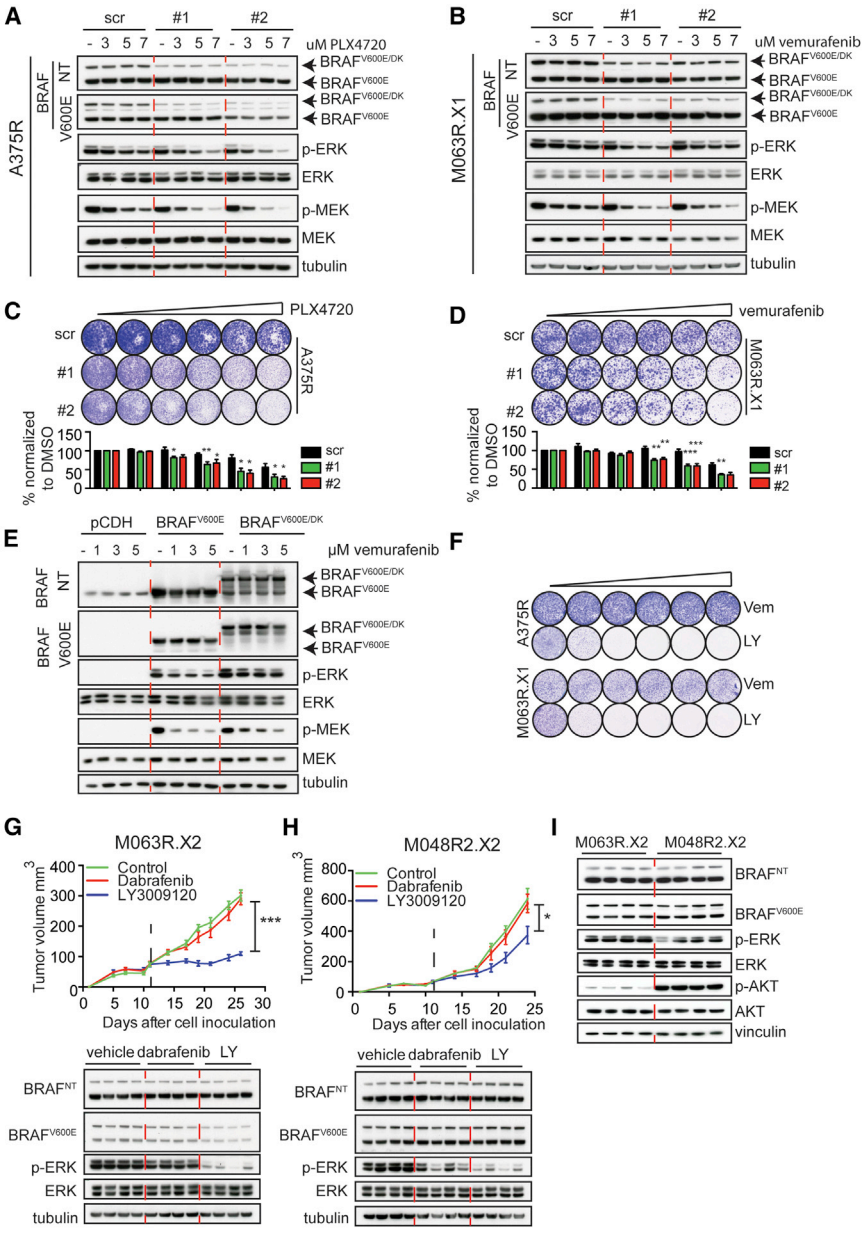

Figure 7. BRAF$^{V600E/DK}$ Is Responsible for Resistance to BRAFi

(A and B) Immunoblotting of A375R (A) or M063R.X1 (B) cells infected with either scrambled shRNAs (scr) or two different shRNAs specifically targeting the BRAF$^{V600E/DK}$. Cells were treated with indicated concentrations of inhibitor.

(C and D) Colony formation assays with A375R (C) or M063R.X1 (D) cells infected with either scrambled shRNAs (scr) or two different shRNAs specifically targeting the BRAF$^{V600E/DK}$-encoding RNA (1 and 2). Cells were treated for 7 days with control vehicle or 1, 3, 5, 7, or 10 μM PLX4720 or vemurafenib. Graphs depict the normalization of six independent experiments. Unpaired t test was performed for each concentration of drug (*$p < 0.05$, **$p < 0.01$, and ***$p < 0.001$). Error bars indicate SEM.

(E) Immunoblotting of HEK293T cells transfected with empty vector or a vector with BRAF^{V600E} or BRAF$^{V600E/DK}$, treated with vehicle or 1, 3, or 5 μM vemurafenib, is shown.

(F) Treatment of A375R and PDX-derived cell line M063R.X1 with increasing concentrations of vemurafenib (0.25–5 μM) or pan-RAF inhibitor LY3009120 (10 nM–1 μM) is shown.

(G and H) Treatment of two PDXs (M048R2.X2 and M063R.X2) that express the BRAF$^{V600E/DK}$ with 30 mg/kg dabrafenib or 15 mg/kg LY3009120 (n = 8 tumors/group). Graphs represent tumor volume and dashed lines indicate start of treatment. Unpaired t test was performed at the last time point (*$p < 0.05$ and ***$p < 0.005$). Error bars indicate SD. Lower part depicts the immunoblotting for p-ERK and BRAF on M048R2.X2 and M063R.X2, treated with either dabrafenib or LY3009120 (each lane represents a tumor derived from an individual mouse).

(I) Immunoblotting for basic levels (vehicle treated) of p-ERK and p-AKT in M063R.X2 and M048R2.X2 (each lane represents a tumor derived from an individual mouse) is shown.

BRAF$^{V600E/DK}$ Melanomas Are Sensitive to Pan-RAF Dimerization Inhibition

Finally, having established that BRAF$^{V600E/DK}$ accounts for BRAFi resistance in melanoma, we wished to identify a treatment capable of targeting cells harboring this mutant. Recently, Peng et al. (2015) have shown that a new pan-RAF dimerization inhibitor (LY3009120) inhibits various forms of BRAF dimers, including the previously described p61 BRAF isoform (Peng et al., 2015; Poulikakos et al., 2011). We treated two cell lines (A375R and PDX-derived cell line M063R.X1), both of which harbored BRAF$^{V600E/DK}$, with LY3009120. Compared to treatment with vemurafenib, these cell lines were highly sensitive to treatment with LY3009120 (Figure 7F).

Next we tested the effect of the LY3009120 compound in vivo, using two PDXs (M063R.X2 and M048R2.X2) that had acquired the BRAF$^{V600E/DK}$ as resistance mechanism (Figure 6A). Both PDXs were treated either with the BRAF inhibitor dabrafenib, to which they were completely resistant (Figures 7G and 7H), or the pan-RAF dimerization inhibitor LY3009120. LY3009120 treatment of M063R.X2 resulted in an effective inhibition of p-ERK and thereby stable disease (Figure 7G). In contrast, upon LY3009120 treatment, M048R2.X2 displayed delayed tumor outgrowth only (Figure 7H). As shown previously, resistance mechanisms in PDX samples can be heterogeneous (Kemper et al., 2015; Van Allen et al., 2014). Moreover, above we described that M048R2.X2 harbors an AKT3^{L51R} mutation in addition to the BRAF$^{V600E/DK}$ mutation (Figure S4C), which conceivably explains the reduced sensitivity to the pan-RAF dimerization inhibitor: the AKT3^{L51R} mutation fuels the PI3K/AKT pathway, which may reduce the effect of BRAFi.

Indeed, AKT signaling was much more active in the M048R2.X2 PDX (Figure 7I), explaining its only partial sensitivity to LY3009120.

These results warrant clinical validation of LY3009120 for treating melanoma patients harboring a $BRAF^{V600E/DK}$ mutation. More generally, these findings highlight one key feature of our PDX platform.

DISCUSSION

Here we present a comprehensive and well-characterized PDX collection comprising 89 metastatic human melanomas, including a set of matched pre-treatment/post-relapse pairs. Tumor tissue for this platform was derived from $BRAF^{V600E}$, $NRAS^{Q61}$, and $BRAF^{WT}$/$NRAS^{WT}$ metastatic melanomas. Samples were acquired before the start of targeted therapy and/or after resistance had occurred. By analyzing biomarker expression, chromosomal aberrations, and RNA expression, we demonstrate that these PDXs recapitulate the key characteristics of the corresponding patients' tumors. In addition, we show that PDXs derived from vemurafenib-resistant melanomas harbor a plethora of established clinical resistance mechanisms: (1) we have identified previously established resistance-causing mutations, amplifications, and protein expression changes in a cohort of treatment-refractory PDXs; (2) we show that resistance to targeted therapy is maintained in PDXs; (3) we present evidence for reversal and adaption of drug response similar to what is seen in the clinic; and (4) we observed genetic heterogeneity in resistance mechanisms in PDXs, similar to what is observed in the clinic. Although not explored here, adding to the versatility of the PDX platform, several fundamental aspects of melanoma progression, like phenotype switching (Hoek et al., 2006; Verfaillie et al., 2015), are better studied in an in vivo setting. Finally, to illustrate the power and utility of this platform, we have taken advantage of its limitless tumor resource, in contrast to patients' biopsies. Screening in PDX cell lysates for BRAF proteins with aberrant molecular weights, we identified a kinase domain duplication mutant of $BRAF^{V600E}$, which drives vemurafenib resistance.

While several resistance mechanisms have been identified previously thanks to the efforts of many laboratories (Nazarian et al., 2010; Paraiso et al., 2011; Poulikakos et al., 2011; Shi et al., 2012, 2014a; Das Thakur et al., 2013; Wagenaar et al., 2014; Wagle et al., 2011), we show here that a specific genetic duplication encoding the kinase domain of $BRAF^{V600E}$ causes resistance to MAPK pathway inhibition. Remarkably, the genomic rearrangement, which results from intronic breaks between exons 9 and 10 and between exons 18 and 19, leaves the original stop codon present in exon 18 intact. As melanoma cells seem to preferentially use the alternative splice donor site in exon 18 to splice to the alternative X1 3′ UTR in exon 19 (and thus use the X1 stop codon) (Marranci et al., 2015), this conceivably explains why cells carrying the genomic duplication of the kinase domain use this splice donor site to produce the $BRAF^{V600E/DK}$ protein. This may imply that the splicing event can be induced by drug exposure; this would provide a selective advantage, whereas expression of $BRAF^{V600E/DK}$ in the absence of BRAFi would not.

Previously, others have shown that duplication of the kinase domain of RTKs, like EGFR (Gallant et al., 2015; Ozer et al., 2010) or FGFR1 (Zhang et al., 2015), drives oncogenicity in glioblastoma, lung cancer, and gliomas, respectively. Recently, wild-type BRAF with a duplicated kinase domain was detected in a neuroblastoma tumor after chemotherapy (Eleveld et al., 2015), but such an event has not yet been implicated in acquired resistance to targeted therapy. Further research will be required to unravel the mechanism of how $BRAF^{V600E/DK}$ functions at a molecular level. Of note, we have attempted to overexpress the $BRAF^{V600E/DK}$ in $BRAF^{V600E}$ and $NRAS^{WT}BRAF^{WT}$ melanoma cell lines, but we observed that cells quickly shut down the expression of this mutant, thereby precluding the study of any functional consequences. Melanomas harboring $BRAF^{V600E/DK}$ to drive resistance have adapted over the course of acquiring resistance to express optimal levels of $BRAF^{V600E}$ and $BRAF^{V600E/DK}$, and perhaps additional rewiring of signaling networks. Apparently, for this particular mutation, this is difficult to recapitulate in the lab by introducing this mutant freshly into melanoma cells that previously were not dependent on it. This is not a general pattern; for example, we have shown previously that ectopic expression of $MEK1^{T55insdelRT}$ is easily achieved and drives drug resistance (Kemper et al., 2015).

Using an inhibitor that targets the $BRAF^{V600E}$ homodimers (Peng et al., 2015), we were able to eliminate $BRAF^{V600E/DK}$ melanoma cells and effectively inhibited tumor growth of PDXs in vivo. As we identified the $BRAF^{V600E/DK}$ as a resistance mechanism in ~10% of PDXs and patient samples, this pan-RAF dimerization inhibitor may offer a clinical opportunity for this particular subgroup of patients who have required resistance to (combined) inhibitors of the BRAF pathway, arguing that screening for this subset of patients could be beneficial.

We conclude that the PDX platform presented here reflects the original melanomas in patients very well with respect to several key characteristics, including resistance mechanisms. This platform therefore provides a relevant and comprehensive suite of well-characterized treatment-naive and -resistant melanomas, representing an invaluable toolbox for studying fundamental aspects of melanoma biology and for the development, validation, and optimization of melanoma (combinatorial) treatments, to further improve the perspective on melanoma patients.

EXPERIMENTAL PROCEDURES

Patient Samples, Animals, and PDXs

The collection and use of human tissue was approved by the Medical Ethical Review Board of the Antoni van Leeuwenhoek. Animal experiments were approved by the animal experimental committee of the institute and performed according to Dutch law. Human tumor tissue was obtained either by excision during surgery or using a 14-gauge biopsy needle. Tumor fragments of ~5 mm^3 were used for subcutaneous transplantation into NSG mice, which was performed under anesthesia. Before reaching the maximum allowed tumor size, mice were sacrificed, tumors were removed, and tumor pieces were (1) fixed in formalin and embedded in paraffin; (2) snap-frozen and stored at −80°C for further analyses; (3) cryopreserved in 10% fetal calf serum (FCS) in DMSO and stored at −80°C for additional passages; and (4) re-transplanted into a new set of NSG mice. Treatment was performed with dabrafenib (Abmole, 30 mg/kg daily) or LY3009120 (Selleck, 15 mg/kg twice daily [b.i.d.]) by oral gavage. Inhibitors were dissolved in DMSO and further diluted in the

vehicle 0.5% hydroxypropylmethylcellulose (Sigma-Aldrich) and 0.2% Tween 80 in (pH 8.0) distilled H_20.

IHC

PDX pieces were fixed in formalin and embedded in paraffin. Slides were stained for H&E, S100 (Z031129, DakoCytomation), gp-100 (MS-264-S0, Thermo Scientific), melanA (M719629, DakoCytomation), tyrosinase (T311, 9319, Cell Signaling Technology), and p-ERK1/2 (E10, 4370, Cell Signaling Technology) by our in-house Animal Pathology facility. The NKI-AVL Core Facility Molecular Pathology & Biobanking (CFMPB) provided the NKI-AVL Biobank patient material and performed the $BRAF^{V600E}$ (VE1, Spring Bioscience) staining according to the manufacturer's protocol.

Immunoblotting and Antibodies

Immunoblotting was performed as described previously (Possik et al., 2014). The following antibodies were used: p-ERK1/2 (E10, 9106), ERK1/2 (9102), p-MEK (41G9, 9154), MEK (L38C12, 4694), p-AKT (D9E, 4060), and p-MET (Tyr1234, 3077) from Cell Signaling Technology; $BRAF^{V600E}$ (VE1) from Spring Bioscience; B-RAF (F7), EGFR (1005), MET (C-28), PDGFR (C20), AXL (C-20), and PTEN (A2B1) from Santa Cruz Biotechnology; MITF (ab12039) from Abcam; and vinculin (V9131) from Sigma.

Cell Culture, Transfection, and Virus Production

Melanoma cell lines and HEK293T cells were cultured in DMEM containing fetal bovine serum (FBS) (Sigma), 2 mM glutamine, 100 U/ml penicillin, and 0.1 mg/ml streptomycin (all Gibco) under standard conditions. Resistant cell lines were generated by treatment with increasing concentrations of PLX4720 (Selleck Chemicals, up to 3 μM) or the combination of dabrafenib (GSK2118436, Abmole, up to 0.5 μM)/trametinib (GSK1120212, S2673, Selleck Chemicals, up to 50 nM). Transfections and production of lentivirus were performed as described previously (Vredeveld et al., 2012). A375R cells were infected and selected with puromycin (1 μg/ml). For the colony formation assays, 20,000 cells were seeded in six-well plates and indicated concentrations of PLX4720, vemurafenib, or LY3009120 were added the next day. Cells were stained by 0.1% crystal violet in 50% methanol and 50% H_20. After staining, de-staining by 10% acetic acid was used to quantify the number of stained cells. Color intensity was measured at 590 nm and values were normalized to DMSO control. For immunoblotting, cells were treated for 24 hr with the indicated concentrations of BRAFi.

qPCR, Sanger Sequencing, and Validation of the Presence/Cloning of $BRAF^{V600E/DK}$ and shRNA Generation

All primers and hairpin sequences are described in Table S7. $BRAF^{V600E/DK}$ was cloned from the 888melDR cell line into a TOPO TA-cloning vector (450071, Invitrogen); we used the restriction site XbaI and SwaI to clone $BRAF^{V600E/D}$ into the pCDH vector. $BRAF^{V600E/DK}$ shRNAs were designed at the junction region between exons 18 and 10.

Statistical Testing

The data of in vivo experiments were analyzed at the last time point by an unpaired t test using the Prism software. For the colony formations assays, six independent experiments were performed. Data were normalized to the scr control for each concentration of the drug. Unpaired t tests were used (in Prism software) to compare the effect between the scr and the two hairpins for each concentration of the drug.

SUPPLEMENTAL INFORMATION

Supplemental Information includes Supplemental Experimental Procedures, seven figures, and seven tables and can be found with this article online at http://dx.doi.org/10.1016/j.celrep.2016.05.064.

AUTHOR CONTRIBUTIONS

K.K., O.K., X.K., and D.S.P. designed and managed all experiments. K.K., X.K., P.C.-S., and A.S. performed all in vitro and in vivo experiments. O.K., T.K., R.J.C.K., and Y.S.J. performed the bio-informatics analysis. O.B.B. and A.F.M.A. performed the mass spectrometry analysis. C.S. was responsible for the RNA sequencing of the patient samples. T.N.M.S., C.U.B., and J.B.H. were responsible for the patient data and the acquisition of the patient samples. F.W. and D.L.v.d.V. performed the volumetric measurements on the computed tomography (CT) scans, which was supervised by E.E.V. D.J.A. and U.M. were responsible for DNA sequencing. K.K., O.K., and D.S.P. wrote the manuscript. All authors revised and approved the manuscript. The project was supervised by D.S.P.

ACKNOWLEDGMENTS

We would like to express our gratitude to the patients and their relatives for their cooperation in this study. We thank Xiaohang Qiao for her assistance with the BRAF IP-mass spectrometry experiment and we thank Ji-Ying Song for assessing the PDX H&E slides. We also acknowledge Iris de Rink, Arno Velds (Central Genomics Facility of the NKI), the NKI High Performance Computing, and the NKI-AVL CFMPB. D.S.P. and K.K. are members of the EuroPDX consortium. This work was financially supported by a grant from the Dutch Cancer Society (NKI-2013-5799; K.K., P.C.-S., J.B.H., and D.S.P.), European Research Council (ERC Synergy Grant "Combat Cancer"; X.K., O.K., and D.S.P.), Netherlands Organization for Scientific Research (NWO) through a VIDI grant (723.012.102, A.F.M.A.) and as part of the National Roadmap Large-scale Research Facilities of the Netherlands (project 184.032.201; O.B.B. and A.F.M.A.), Cancer Research UK and The Wellcome Trust (WT098051, D.J.A.), The Josephine Nefkins Foundation (E.E.V.) and Barcode for Life (E.E.V.), and a Queen Wilhelmina Award by the Dutch Cancer Society (D.S.P.).

Received: November 24, 2015
Revised: April 8, 2016
Accepted: May 16, 2016
Published: June 16, 2016

REFERENCES

Basile, K.J., Abel, E.V., and Aplin, A.E. (2012). Adaptive upregulation of FOXD3 and resistance to PLX4032/4720-induced cell death in mutant B-RAF melanoma cells. Oncogene *31*, 2471–2479.

Bertotti, A., Migliardi, G., Galimi, F., Sassi, F., Torti, D., Isella, C., Corà, D., Di Nicolantonio, F., Buscarino, M., Petti, C., et al. (2011). A molecularly annotated platform of patient-derived xenografts ("xenopatients") identifies HER2 as an effective therapeutic target in cetuximab-resistant colorectal cancer. Cancer Discov. *1*, 508–523.

Burchill, S.A. (2006). What do, can and should we learn from models to evaluate potential anticancer agents? Future Oncol. *2*, 201–211.

Cancer Genome Atlas Network (2015). Genomic classification of cutaneous melanoma. Cell *161*, 1681–1696.

Chapman, P.B., Hauschild, A., Robert, C., Haanen, J.B., Ascierto, P., Larkin, J., Dummer, R., Garbe, C., Testori, A., Maio, M., et al.; BRIM-3 Study Group (2011). Improved survival with vemurafenib in melanoma with BRAF V600E mutation. N. Engl. J. Med. *364*, 2507–2516.

Clement, V., Sanchez, P., de Tribolet, N., Radovanovic, I., and Ruiz i Altaba, A. (2007). HEDGEHOG-GLI1 signaling regulates human glioma growth, cancer stem cell self-renewal, and tumorigenicity. Curr. Biol. *17*, 165–172.

Daniel, V.C., Marchionni, L., Hierman, J.S., Rhodes, J.T., Devereux, W.L., Rudin, C.M., Yung, R., Parmigiani, G., Dorsch, M., Peacock, C.D., and Watkins, D.N. (2009). A primary xenograft model of small-cell lung cancer reveals irreversible changes in gene expression imposed by culture in vitro. Cancer Res. *69*, 3364–3373.

Das Thakur, M., Salangsang, F., Landman, A.S., Sellers, W.R., Pryer, N.K., Levesque, M.P., Dummer, R., McMahon, M., and Stuart, D.D. (2013). Modelling vemurafenib resistance in melanoma reveals a strategy to forestall drug resistance. Nature *494*, 251–255.

Davies, H., Bignell, G.R., Cox, C., Stephens, P., Edkins, S., Clegg, S., Teague, J., Woffendin, H., Garnett, M.J., Bottomley, W., et al. (2002). Mutations of the BRAF gene in human cancer. Nature *417*, 949–954.

De Witt Hamer, P.C., Van Tilborg, A.A.G., Eijk, P.P., Sminia, P., Troost, D., Van Noorden, C.J.F., Ylstra, B., and Leenstra, S. (2008). The genomic profile of human malignant glioma is altered early in primary cell culture and preserved in spheroids. Oncogene *27*, 2091–2096.

DeRose, Y.S., Wang, G., Lin, Y.-C., Bernard, P.S., Buys, S.S., Ebbert, M.T.W., Factor, R., Matsen, C., Milash, B.A., Nelson, E., et al. (2011). Tumor grafts derived from women with breast cancer authentically reflect tumor pathology, growth, metastasis and disease outcomes. Nat. Med. *17*, 1514–1520.

Einarsdottir, B.O., Bagge, R.O., Bhadury, J., Jespersen, H., Mattsson, J., Nilsson, L.M., Truvé, K., López, M.D., Naredi, P., Nilsson, O., et al. (2014). Melanoma patient-derived xenografts accurately model the disease and develop fast enough to guide treatment decisions. Oncotarget *5*, 9609–9618.

Eleveld, T.F., Oldridge, D.A., Bernard, V., Koster, J., Daage, L.C., Diskin, S.J., Schild, L., Bentahar, N.B., Bellini, A., Chicard, M., et al. (2015). Relapsed neuroblastomas show frequent RAS-MAPK pathway mutations. Nat. Genet. *47*, 864–871.

Flaherty, K.T., Puzanov, I., Kim, K.B., Ribas, A., McArthur, G.A., Sosman, J.A., O'Dwyer, P.J., Lee, R.J., Grippo, J.F., Nolop, K., and Chapman, P.B. (2010). Inhibition of mutated, activated BRAF in metastatic melanoma. N. Engl. J. Med. *363*, 809–819.

Gallant, J.-N., Sheehan, J.H., Shaver, T.M., Bailey, M., Lipson, D., Chandramohan, R., Red Brewer, M., York, S.J., Kris, M.G., Pietenpol, J.A., et al. (2015). EGFR kinase domain duplication (EGFR-KDD) is a novel oncogenic driver in lung cancer that is clinically responsive to afatinib. Cancer Discov. *5*, 1155–1163.

Gao, H., Korn, J.M., Ferretti, S., Monahan, J.E., Wang, Y., Singh, M., Zhang, C., Schnell, C., Yang, G., Zhang, Y., et al. (2015). High-throughput screening using patient-derived tumor xenografts to predict clinical trial drug response. Nat. Med. *21*, 1318–1325.

Garraway, L.A., Widlund, H.R., Rubin, M.A., Getz, G., Berger, A.J., Ramaswamy, S., Beroukhim, R., Milner, D.A., Granter, S.R., Du, J., et al. (2005). Integrative genomic analyses identify MITF as a lineage survival oncogene amplified in malignant melanoma. Nature *436*, 117–122.

Girotti, M.R., Gremel, G., Lee, R., Galvani, E., Rothwell, D., Viros, A., Mandal, A.K., Lim, K.H.J., Saturno, G., Furney, S.J., et al. (2016). Application of sequencing, liquid biopsies, and patient-derived xenografts for personalized medicine in melanoma. Cancer Discov. *6*, 286–299.

Hoek, K.S., Schlegel, N.C., Brafford, P., Sucker, A., Ugurel, S., Kumar, R., Weber, B.L., Nathanson, K.L., Phillips, D.J., Herlyn, M., et al. (2006). Metastatic potential of melanomas defined by specific gene expression profiles with no BRAF signature. Pigment Cell Res. *19*, 290–302.

Hugo, W., Shi, H., Sun, L., Piva, M., Song, C., Kong, X., Moriceau, G., Hong, A., Dahlman, K.B., Johnson, D.B., et al. (2015). Non-genomic and immune evolution of melanoma acquiring MAPKi resistance. Cell *162*, 1271–1285.

Kemper, K., Krijgsman, O., Cornelissen-Steijger, P., Shahrabi, A., Weeber, F., Song, J.-Y., Kuilman, T., Vis, D.J., Wessels, L.F., Voest, E.E., et al. (2015). Intra- and inter-tumor heterogeneity in a vemurafenib-resistant melanoma patient and derived xenografts. EMBO Mol. Med. *7*, 1104–1118.

Konieczkowski, D.J., Johannessen, C.M., Abudayyeh, O., Kim, J.W., Cooper, Z.A., Piris, A., Frederick, D.T., Barzily-Rokni, M., Straussman, R., Haq, R., et al. (2014). A melanoma cell state distinction influences sensitivity to MAPK pathway inhibitors. Cancer Discov. *4*, 816–827.

Kuilman, T., Velds, A., Kemper, K., Ranzani, M., Bombardelli, L., Hoogstraat, M., Nevedomskaya, E., Xu, G., de Ruiter, J., Lolkema, M.P., et al. (2015). CopywriteR: DNA copy number detection from off-target sequence data. Genome Biol. *16*, 49.

Larkin, J., Ascierto, P.A., Dréno, B., Atkinson, V., Liszkay, G., Maio, M., Mandalà, M., Demidov, L., Stroyakovskiy, D., Thomas, L., et al. (2014). Combined vemurafenib and cobimetinib in BRAF-mutated melanoma. N. Engl. J. Med. *371*, 1867–1876.

Marranci, A., Tuccoli, A., Vitiello, M., Mercoledi, E., Sarti, S., Lubrano, S., Evangelista, M., Fogli, A., Valdes, C., Russo, F., et al. (2015). Identification of BRAF 3'UTR Isoforms in Melanoma. J. Invest. Dermatol. *135*, 1694–1697.

Monsma, D.J., Monks, N.R., Cherba, D.M., Dylewski, D., Eugster, E., Jahn, H., Srikanth, S., Scott, S.B., Richardson, P.J., Everts, R.E., et al. (2012). Genomic characterization of explant tumorgraft models derived from fresh patient tumor tissue. J. Transl. Med. *10*, 125.

Monsma, D.J., Cherba, D.M., Eugster, E.E., Dylewski, D.L., Davidson, P.T., Peterson, C.A., Borgman, A.S., Winn, M.E., Dykema, K.J., Webb, C.P., et al. (2015). Melanoma patient derived xenografts acquire distinct Vemurafenib resistance mechanisms. Am. J. Cancer Res. *5*, 1507–1518.

Müller, J., Krijgsman, O., Tsoi, J., Robert, L., Hugo, W., Song, C., Kong, X., Possik, P.A., Cornelissen-Steijger, P.D.M., Foppen, M.H.G., et al. (2014). Low MITF/AXL ratio predicts early resistance to multiple targeted drugs in melanoma. Nat. Commun. *5*, 5712.

Nazarian, R., Shi, H., Wang, Q., Kong, X., Koya, R.C., Lee, H., Chen, Z., Lee, M.-K., Attar, N., Sazegar, H., et al. (2010). Melanomas acquire resistance to B-RAF(V600E) inhibition by RTK or N-RAS upregulation. Nature *468*, 973–977.

Nikolaev, S.I., Rimoldi, D., Iseli, C., Valsesia, A., Robyr, D., Gehrig, C., Harshman, K., Guipponi, M., Bukach, O., Zoete, V., et al. (2011). Exome sequencing identifies recurrent somatic MAP2K1 and MAP2K2 mutations in melanoma. Nat. Genet. *44*, 133–139.

Ozer, B.H., Wiepz, G.J., and Bertics, P.J. (2010). Activity and cellular localization of an oncogenic glioblastoma multiforme-associated EGF receptor mutant possessing a duplicated kinase domain. Oncogene *29*, 855–864.

Paraiso, K.H.T., Xiang, Y., Rebecca, V.W., Abel, E.V., Chen, Y.A., Munko, A.C., Wood, E., Fedorenko, I.V., Sondak, V.K., Anderson, A.R.A., et al. (2011). PTEN loss confers BRAF inhibitor resistance to melanoma cells through the suppression of BIM expression. Cancer Res. *71*, 2750–2760.

Parikh, C., Janakiraman, V., Wu, W.-I., Foo, C.K., Kljavin, N.M., Chaudhuri, S., Stawiski, E., Lee, B., Lin, J., Li, H., et al. (2012). Disruption of PH-kinase domain interactions leads to oncogenic activation of AKT in human cancers. Proc. Natl. Acad. Sci. USA *109*, 19368–19373.

Peng, S.-B., Henry, J.R., Kaufman, M.D., Lu, W.-P., Smith, B.D., Vogeti, S., Rutkoski, T.J., Wise, S., Chun, L., Zhang, Y., et al. (2015). Inhibition of RAF Isoforms and Active Dimers by LY3009120 Leads to Anti-tumor Activities in RAS or BRAF Mutant Cancers. Cancer Cell *28*, 384–398.

Possik, P.A., Müller, J., Gerlach, C., Kenski, J.C.N., Huang, X., Shahrabi, A., Krijgsman, O., Song, J.-Y., Smit, M.A., Gerritsen, B., et al. (2014). Parallel in vivo and in vitro melanoma RNAi dropout screens reveal synthetic lethality between hypoxia and DNA damage response inhibition. Cell Rep. *9*, 1375–1386.

Poulikakos, P.I., Persaud, Y., Janakiraman, M., Kong, X., Ng, C., Moriceau, G., Shi, H., Atefi, M., Titz, B., Gabay, M.T., et al. (2011). RAF inhibitor resistance is mediated by dimerization of aberrantly spliced BRAF(V600E). Nature *480*, 387–390.

Robert, C., Karaszewska, B., Schachter, J., Rutkowski, P., Mackiewicz, A., Stroiakovski, D., Lichinitser, M., Dummer, R., Grange, F., Mortier, L., et al. (2015). Improved overall survival in melanoma with combined dabrafenib and trametinib. N. Engl. J. Med. *372*, 30–39.

Rubio-Viqueira, B., Jimeno, A., Cusatis, G., Zhang, X., Iacobuzio-Donahue, C., Karikari, C., Shi, C., Danenberg, K., Danenberg, P.V., Kuramochi, H., et al. (2006). An in vivo platform for translational drug development in pancreatic cancer. Clin. Cancer Res. *12*, 4652–4661.

Shi, H., Moriceau, G., Kong, X., Lee, M.-K., Lee, H., Koya, R.C., Ng, C., Chodon, T., Scolyer, R.A., Dahlman, K.B., et al. (2012). Melanoma whole-exome sequencing identifies (V600E)B-RAF amplification-mediated acquired B-RAF inhibitor resistance. Nat. Commun. *3*, 724.

Shi, H., Hong, A., Kong, X., Koya, R.C., Song, C., Moriceau, G., Hugo, W., Yu, C.C., Ng, C., Chodon, T., et al. (2014a). A novel AKT1 mutant amplifies an adaptive melanoma response to BRAF inhibition. Cancer Discov. *4*, 69–79.

Shi, H., Hugo, W., Kong, X., Hong, A., Koya, R.C., Moriceau, G., Chodon, T., Guo, R., Johnson, D.B., Dahlman, K.B., et al. (2014b). Acquired resistance

and clonal evolution in melanoma during BRAF inhibitor therapy. Cancer Discov. *4*, 80–93.

Solit, D.B., and Rosen, N. (2014). Towards a unified model of RAF inhibitor resistance. Cancer Discov. *4*, 27–30.

Straussman, R., Morikawa, T., Shee, K., Barzily-Rokni, M., Qian, Z.R., Du, J., Davis, A., Mongare, M.M., Gould, J., Frederick, D.T., et al. (2012). Tumour micro-environment elicits innate resistance to RAF inhibitors through HGF secretion. Nature *487*, 500–504.

Sun, C., Wang, L., Huang, S., Heynen, G.J.J.E., Prahallad, A., Robert, C., Haanen, J., Blank, C., Wesseling, J., Willems, S.M., et al. (2014). Reversible and adaptive resistance to BRAF(V600E) inhibition in melanoma. Nature *508*, 118–122.

Van Allen, E.M., Wagle, N., Sucker, A., Treacy, D.J., Johannessen, C.M., Goetz, E.M., Place, C.S., Taylor-Weiner, A., Whittaker, S., Kryukov, G.V., et al.; Dermatologic Cooperative Oncology Group of Germany (DeCOG) (2014). The genetic landscape of clinical resistance to RAF inhibition in metastatic melanoma. Cancer Discov. *4*, 94–109.

Verfaillie, A., Imrichova, H., Atak, Z.K., Dewaele, M., Rambow, F., Hulselmans, G., Christiaens, V., Svetlichnyy, D., Luciani, F., Van den Mooter, L., et al. (2015). Decoding the regulatory landscape of melanoma reveals TEADS as regulators of the invasive cell state. Nat. Commun. *6*, 6683.

Vergani, E., Vallacchi, V., Frigerio, S., Deho, P., Mondellini, P., Perego, P., Cassinelli, G., Lanzi, C., Testi, M.A., Rivoltini, L., et al. (2011). Identification of MET and SRC activation in melanoma cell lines showing primary resistance to PLX4032. Neoplasia *13*, 1132–1142.

Voskoglou-Nomikos, T., Pater, J.L., and Seymour, L. (2003). Clinical predictive value of the in vitro cell line, human xenograft, and mouse allograft preclinical cancer models. Clin. Cancer Res. *9*, 4227–4239.

Vredeveld, L.C.W., Possik, P.A., Smit, M.A., Meissl, K., Michaloglou, C., Horlings, H.M., Ajouaou, A., Kortman, P.C., Dankort, D., McMahon, M., et al. (2012). Abrogation of BRAFV600E-induced senescence by PI3K pathway activation contributes to melanomagenesis. Genes Dev. *26*, 1055–1069.

Wagenaar, T.R., Ma, L., Roscoe, B., Park, S.M., Bolon, D.N., and Green, M.R. (2014). Resistance to vemurafenib resulting from a novel mutation in the BRAFV600E kinase domain. Pigment Cell Melanoma Res. *27*, 124–133.

Wagle, N., Emery, C., Berger, M.F., Davis, M.J., Sawyer, A., Pochanard, P., Kehoe, S.M., Johannessen, C.M., Macconaill, L.E., Hahn, W.C., et al. (2011). Dissecting therapeutic resistance to RAF inhibition in melanoma by tumor genomic profiling. J. Clin. Oncol. *29*, 3085–3096.

Wagle, N., Van Allen, E.M., Treacy, D.J., Frederick, D.T., Cooper, Z.A., Taylor-Weiner, A., Rosenberg, M., Goetz, E.M., Sullivan, R.J., Farlow, D.N., et al. (2014). MAP kinase pathway alterations in BRAF-mutant melanoma patients with acquired resistance to combined RAF/MEK inhibition. Cancer Discov. *4*, 61–68.

Zhang, L., Zhou, Y., Cheng, C., Cui, H., Cheng, L., Kong, P., Wang, J., Li, Y., Chen, W., Song, B., et al. (2015). Genomic analyses reveal mutational signatures and frequently altered genes in esophageal squamous cell carcinoma. Am. J. Hum. Genet. *96*, 597–611.

Cell Reports, Volume *16*

Supplemental Information

$BRAF^{V600E}$ Kinase Domain Duplication Identified in Therapy-Refractory Melanoma Patient-Derived Xenografts

Kristel Kemper, Oscar Krijgsman, Xiangjun Kong, Paulien Cornelissen-Steijger, Aida Shahrabi, Fleur Weeber, Daphne L. van der Velden, Onno B. Bleijerveld, Thomas Kuilman, Roel J.C. Kluin, Chong Sun, Emile E. Voest, Young Seok Ju, Ton N.M. Schumacher, A.F. Maarten Altelaar, Ultan McDermott, David J. Adams, Christian U. Blank, John B. Haanen, and Daniel S. Peeper

Figure S1

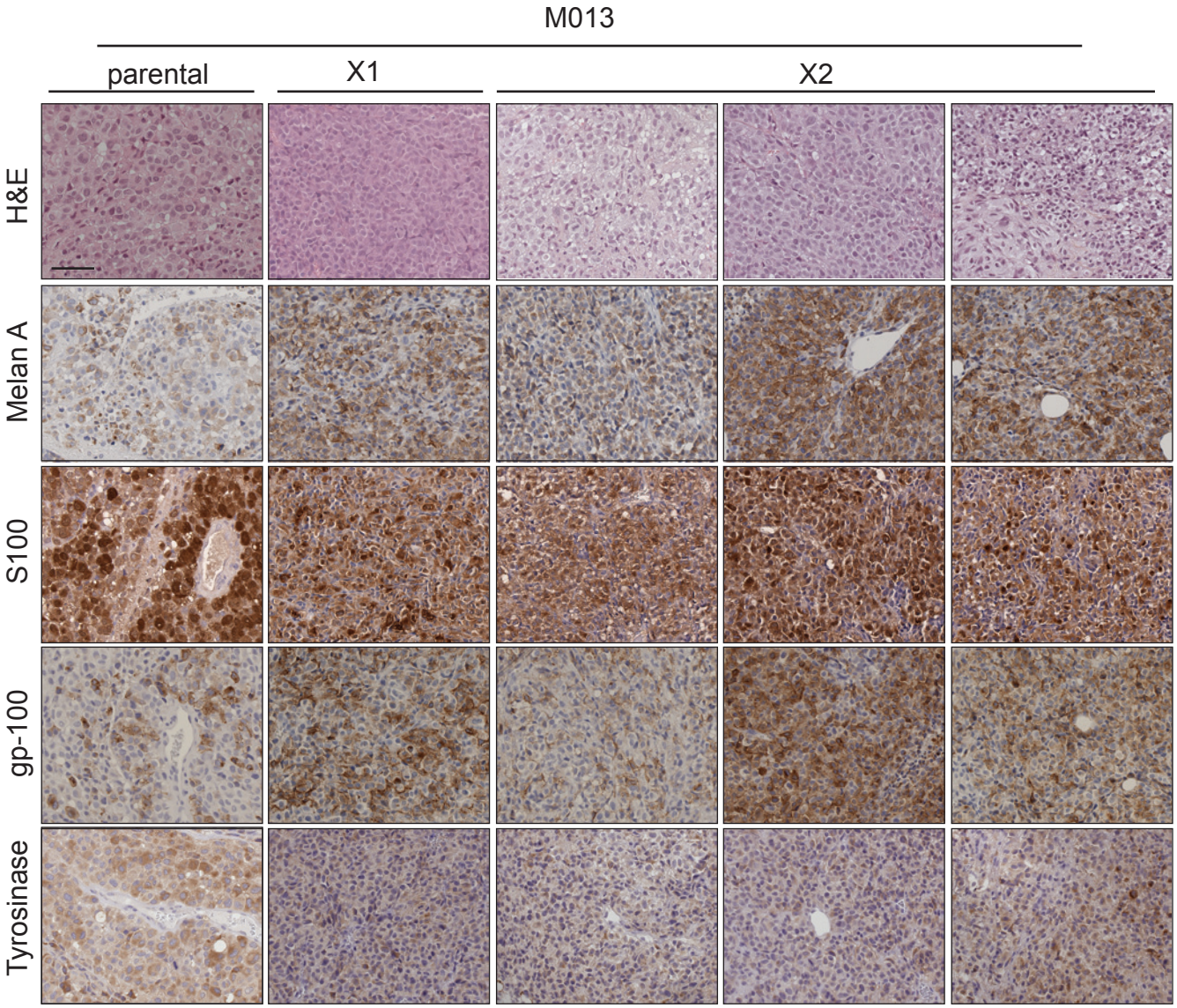

Figure S2

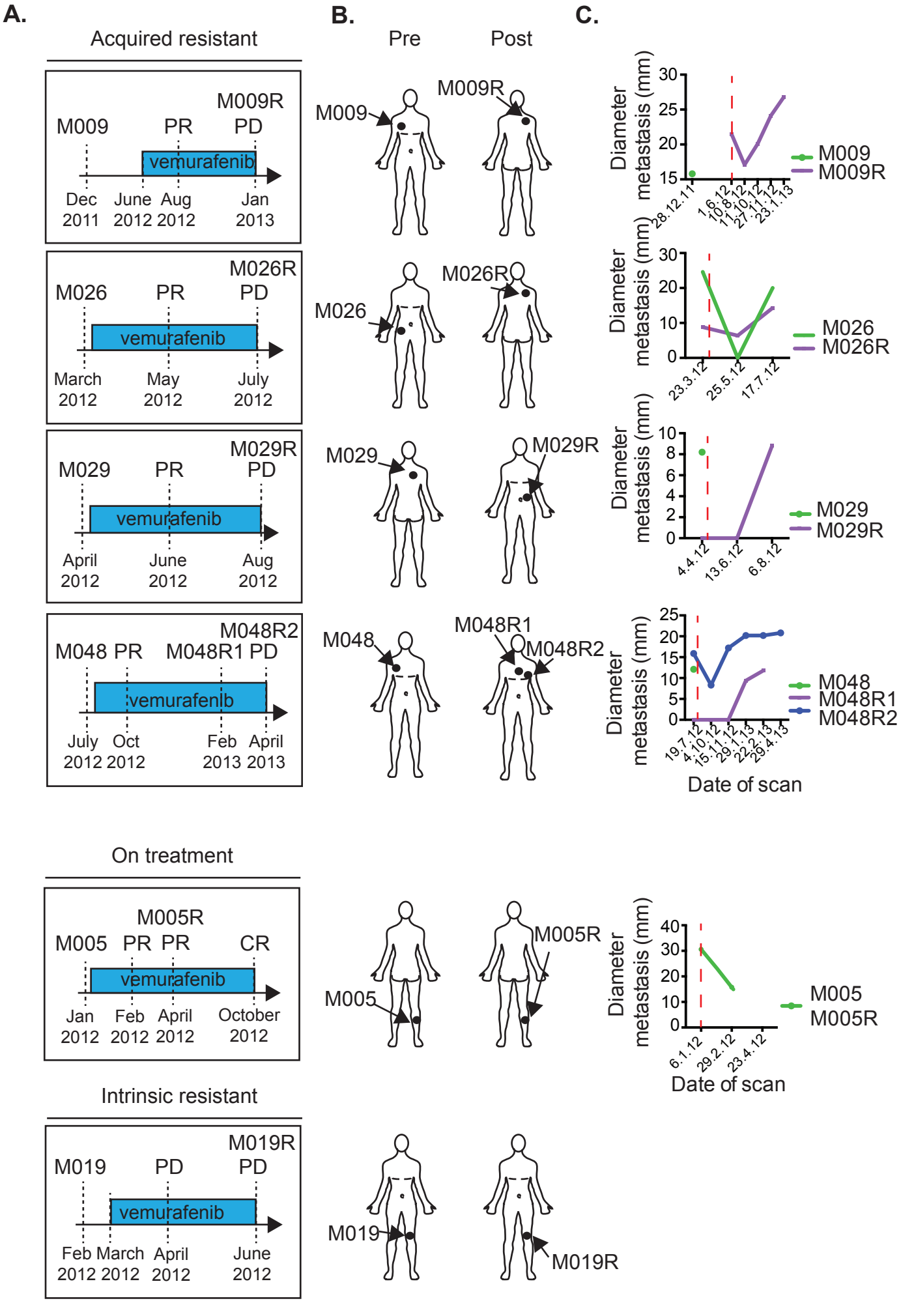
A.
B.
C.
Acquired resistant
Pre
Post
M009
PR
M009R
PD
vemurafenib
Dec 2011
June 2012
Aug 2012
Jan 2013
M026
M026R
March 2012
May 2012
July 2012
M029
M029R
April 2012
June 2012
Aug 2012
M048
PR
M048R1
PD
M048R2
July 2012
Oct 2012
Feb 2013
April 2013
Diameter metastasis (mm)
28.12.11
1.6.12
10.8.12
11.10.12
27.11.12
23.1.13
23.3.12
25.5.12
17.7.12
4.4.12
13.6.12
6.8.12
19.7.12
4.10.12
15.11.12
29.1.13
22.2.13
29.4.13
Date of scan
On treatment
M005
M005R
Jan 2012
Feb 2012
April 2012
October 2012
6.1.12
29.2.12
23.4.12
Intrinsic resistant
M019
M019R
Feb 2012
March 2012
April 2012
June 2012

Figure S3

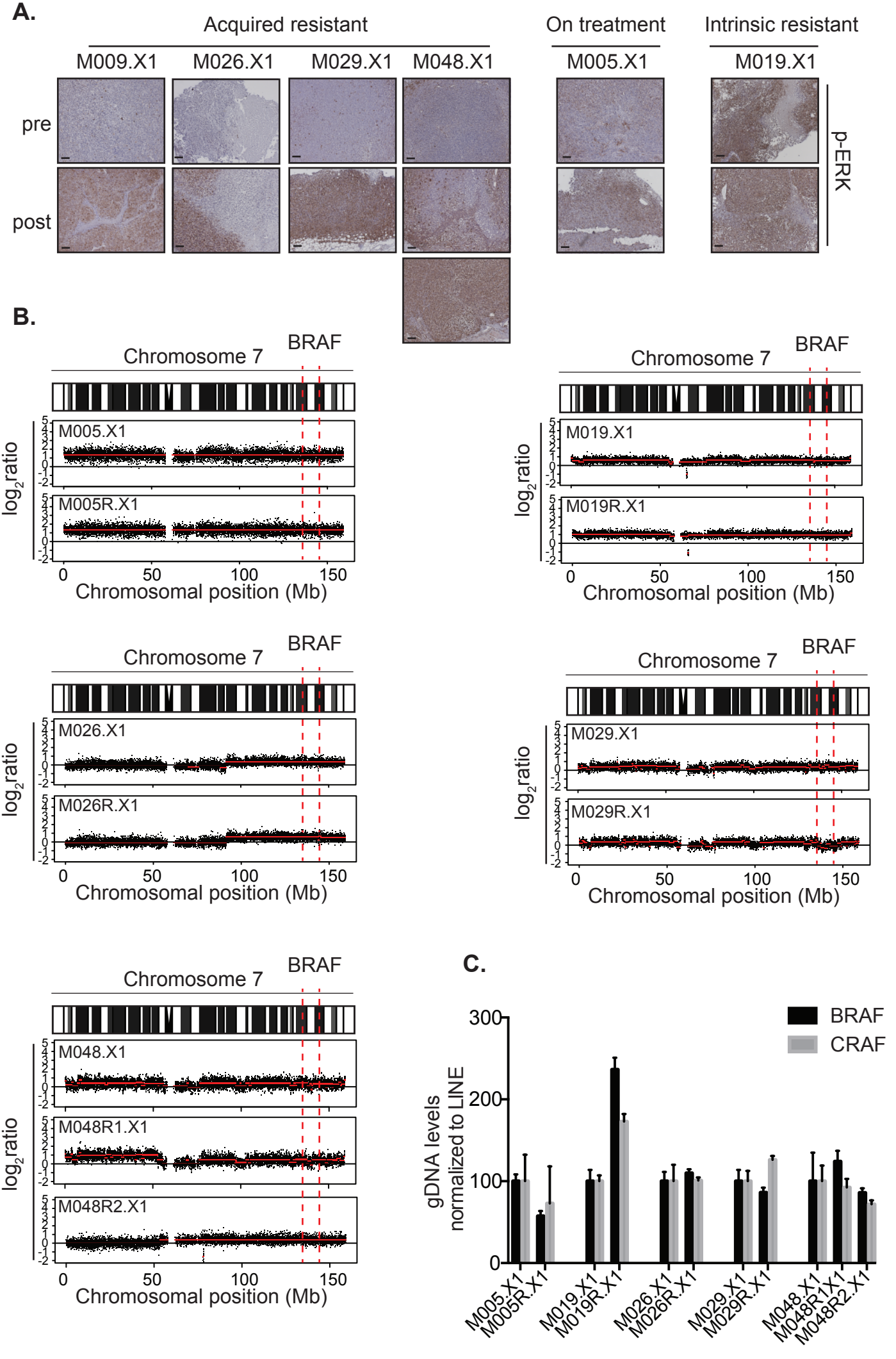
A.
Acquired resistant
On treatment
Intrinsic resistant
M009.X1
M026.X1
M029.X1
M048.X1
M005.X1
M019.X1
pre
post
p-ERK
B.
Chromosome 7
BRAF
M005.X1
M005R.X1
M019.X1
M019R.X1
M026.X1
M026R.X1
M029.X1
M029R.X1
M048.X1
M048R1.X1
M048R2.X1
log2ratio
Chromosomal position (Mb)
C.
gDNA levels normalized to LINE
BRAF
CRAF
M005.X1
M005R.X1
M019.X1
M019R.X1
M026.X1
M026R.X1
M029.X1
M029R.X1
M048.X1
M048R1X1
M048R2.X1

Figure S4

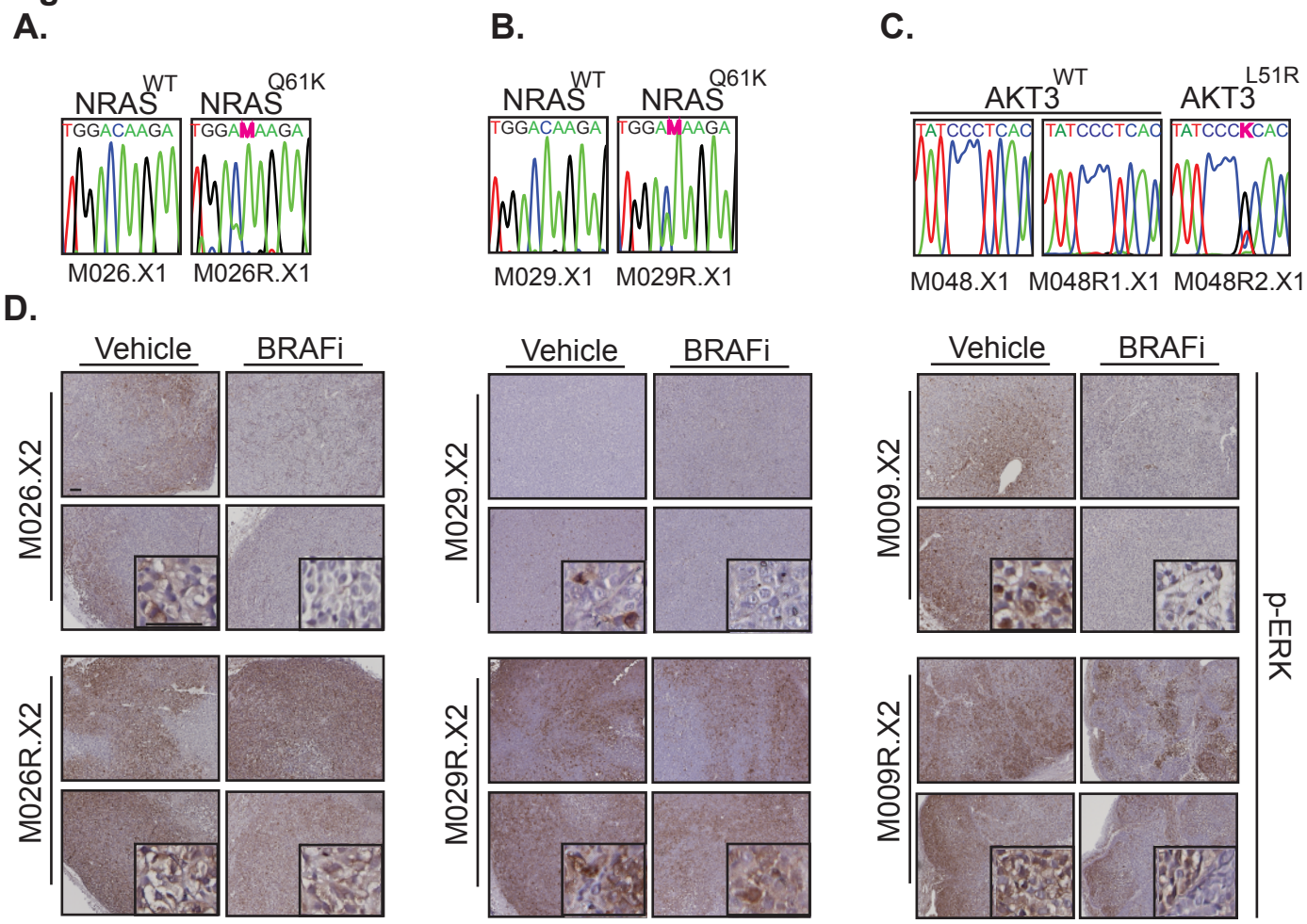
A.
NRAS WT
NRAS Q61K
TGGACAAGA
TGGAMAAGA
M026.X1
M026R.X1
B.
NRAS WT
NRAS Q61K
TGGACAAGA
TGGAMAAGA
M029.X1
M029R.X1
C.
AKT3 WT
AKT3 L51R
TATCCCTCAC
TATCCCTCAC
TATCCCKCAC
M048.X1
M048R1.X1
M048R2.X1
D.
Vehicle
BRAFi
M026.X2
M026R.X2
M029.X2
M029R.X2
M009.X2
M009R.X2
p-ERK

Figure S5

A.

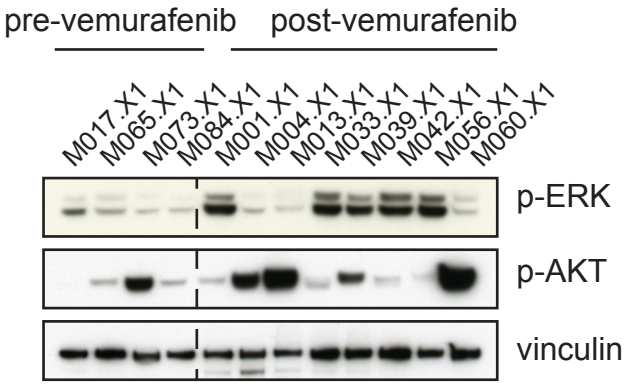
pre-vemurafenib
post-vemurafenib
M017.X1
M065.X1
M073.X1
M084.X1
M001.X1
M004.X1
M013.X1
M033.X1
M039.X1
M042.X1
M056.X1
M060.X1
p-ERK
p-AKT
vinculin

B.

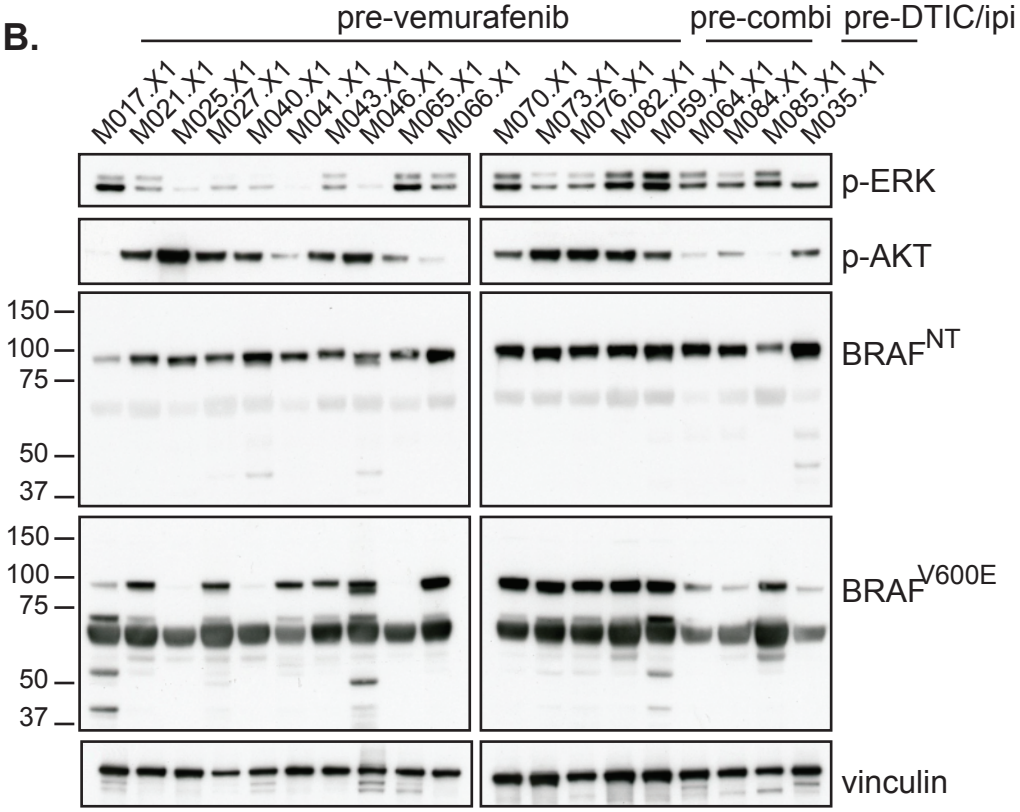
pre-vemurafenib
pre-combi
pre-DTIC/ipi
M017.X1
M021.X1
M025.X1
M027.X1
M040.X1
M041.X1
M043.X1
M046.X1
M065.X1
M066.X1
M070.X1
M073.X1
M076.X1
M082.X1
M059.X1
M064.X1
M084.X1
M085.X1
M035.X1
p-ERK
p-AKT
150
100
75
50
37
BRAF^NT
150
100
75
50
37
BRAF^V600E
vinculin

Figure S6

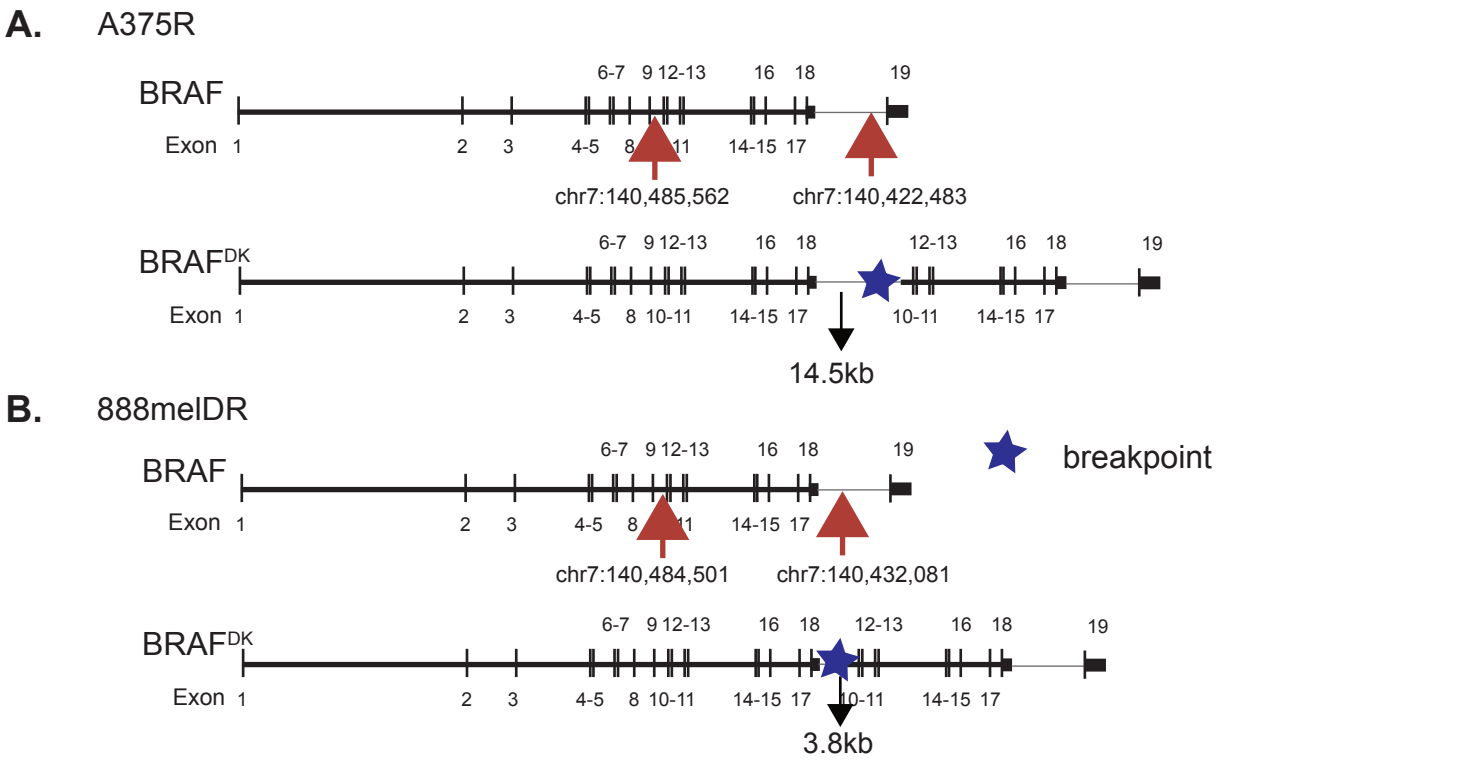
A.
A375R
BRAF
Exon 1 2 3 4-5 8 11 14-15 17
6-7 9 12-13 16 18 19
chr7:140,485,562
chr7:140,422,483
BRAFDK
Exon 1 2 3 4-5 8 10-11 14-15 17 10-11 14-15 17
6-7 9 12-13 16 18 12-13 16 18 19
14.5kb
B.
888melDR
BRAF
Exon 1 2 3 4-5 8 11 14-15 17
6-7 9 12-13 16 18 19
breakpoint
chr7:140,484,501
chr7:140,432,081
BRAFDK
Exon 1 2 3 4-5 8 10-11 14-15 17 10-11 14-15 17
6-7 9 12-13 16 18 12-13 16 18 19
3.8kb

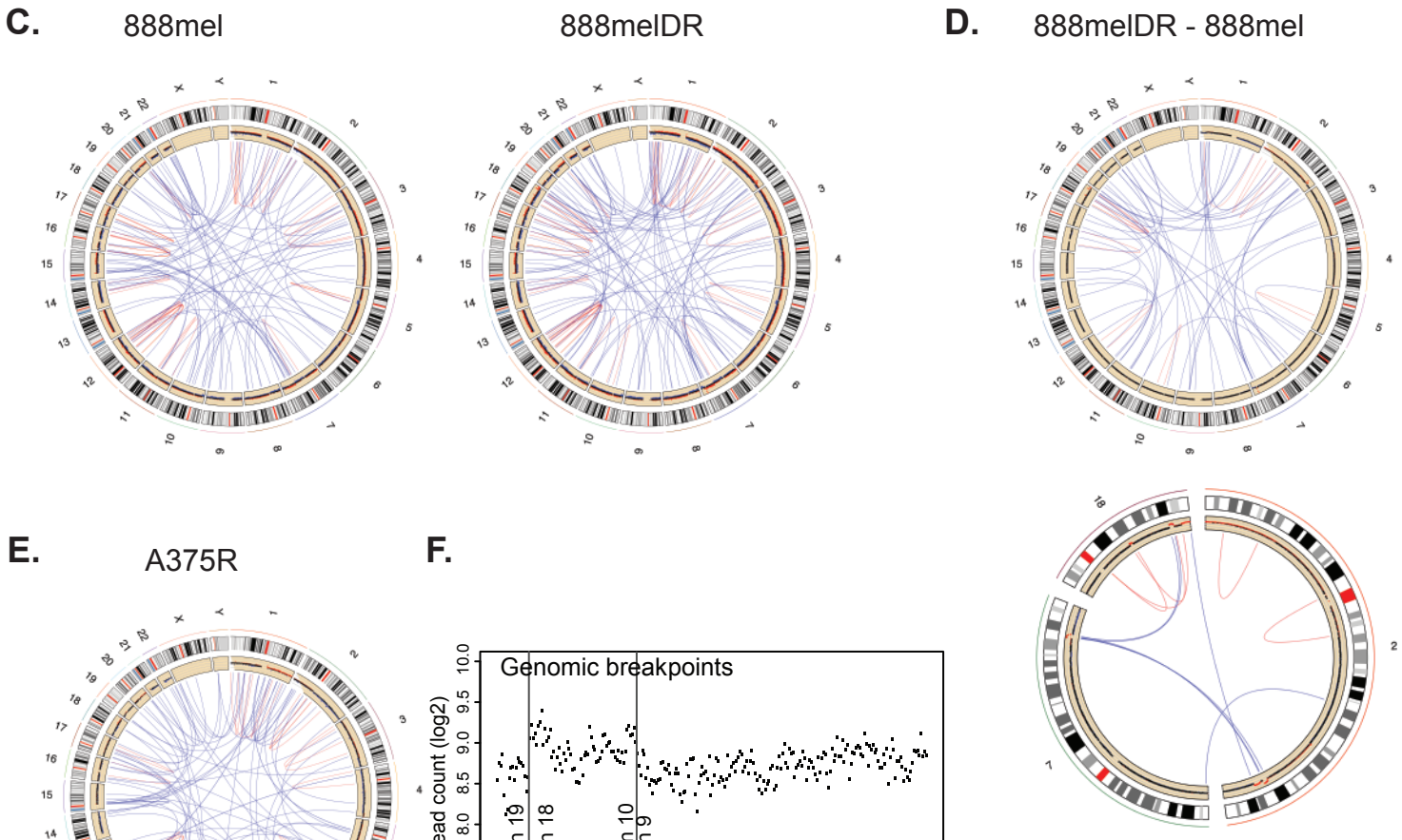
C.
888mel
888melDR
D.
888melDR - 888mel

E.
A375R
F.
Genomic breakpoints
Read count (log2)
7.0 7.5 8.0 8.5 9.0 9.5 10.0
exon 19
exon 18
exon 10
exon 9
BRAF
140.4 140.5 140.6
Genomic location (Mb)

Figure S7

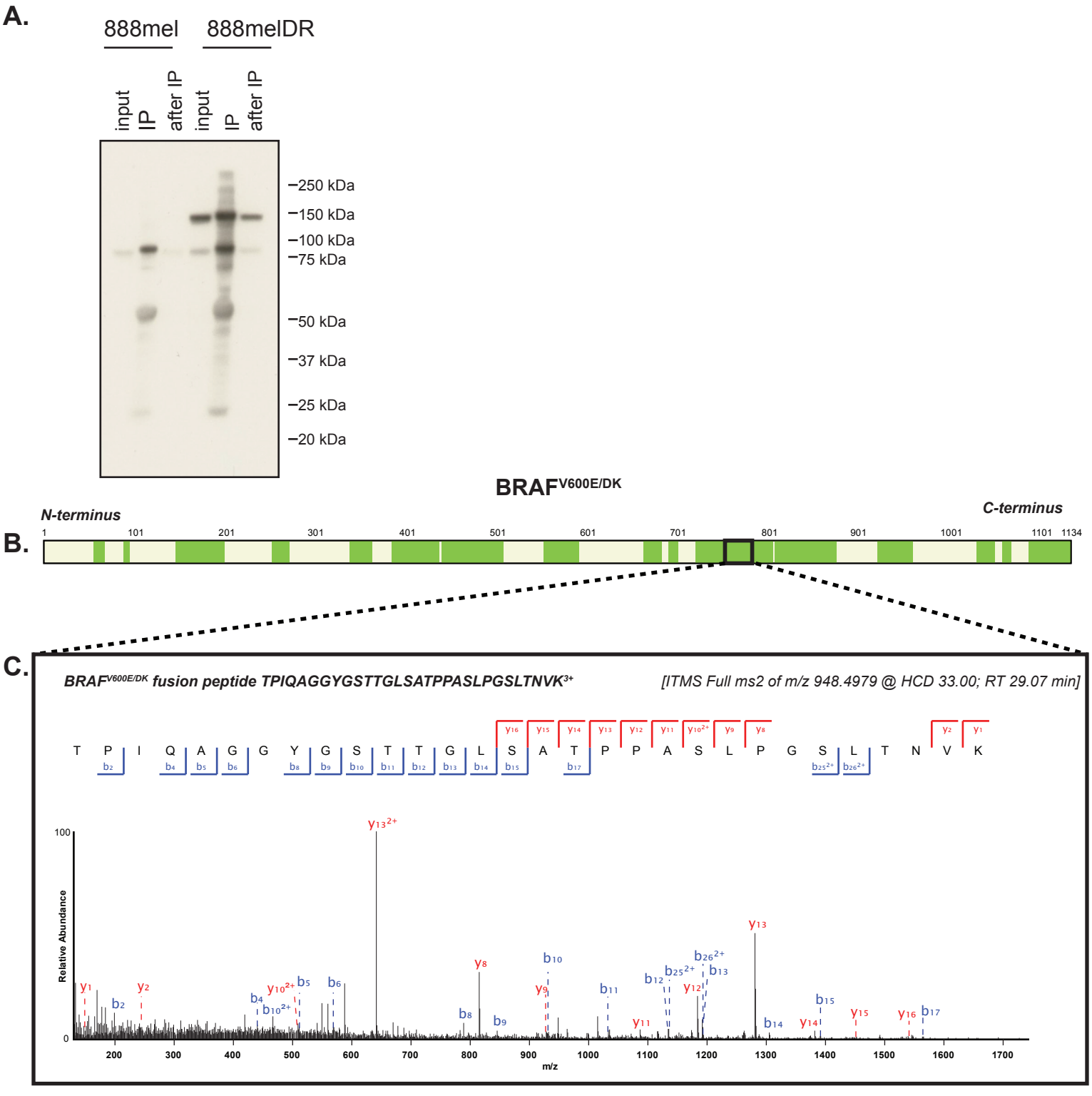
A.
888mel
888melDR
input
IP
after IP
input
IP
after IP
250 kDa
150 kDa
100 kDa
75 kDa
50 kDa
37 kDa
25 kDa
20 kDa
B.
BRAF V600E/DK
N-terminus
C-terminus
1
101
201
301
401
501
601
701
801
901
1001
1101
1134
C.
BRAF V600E/DK fusion peptide TPIQAGGYGSTTGLSATPPASLPGSLTNVK 3+
[ITMS Full ms2 of m/z 948.4979 @ HCD 33.00; RT 29.07 min]
T P I Q A G G Y G S T T G L S A T P P A S L P G S L T N V K
Relative Abundance
m/z
100
0
200
300
400
500
600
700
800
900
1000
1100
1200
1300
1400
1500
1600
1700

Supplemental Figure legends:

Figure S1. Stable marker expression upon *in vivo* passaging of melanoma PDX, Related to Figure 1.
H&E stainings and IHC stainings for MelanA, S100, gp-100 and tyrosinase were performed on the parental tumor and two subsequent passages of PDX (X1 and X2). Scale bars indicate 100 μm.

Figure S2. Clinical histories of patients from matched pre- and post-vemurafenib PDX pairs, Related to Figure 2.
A. Vemurafenib treatment schedule for each patient from whom we obtained tumor specimens before start of treatment, during treatment or after resistance had occurred. Indicated are the time points when the samples were taken. The overall response, according to RECIST 1.1 criteria, is indicated. **B.** Location of each of the obtained patient samples. **C.** For each individual lesion, the diameter was measured at baseline (before start of treatment) and every two consecutive months during treatment until progressive disease was observed. For one patient (M019), the CT-scans of the tumor location were unavailable. Vertical dashed line indicates start of vemurafenib treatment. For three patients (M009, M029, M048), the pre-treatment PDX were derived from lesions that were surgically removed before the start of treatment and these tumors did not recur at those particular locations. One pre-treatment PDX was derived from a lesion that showed a complete response (CR) to vemurafenib before it recurred (M026) According to the response data, we have grouped these PDX pairs in 1) acquired resistant 2) on treatment and 3) intrinsic resistant.

Figure S3. BRAF amplification was not detected in the other matched PDX pairs, Related to Figure 2.
A. Staining for p-ERK on FFPE archival material of the matched PDX pairs. Scale bars indicate 100 μm. **B.** No amplification of the genomic region containing BRAF was identified in any of the matched PDX pairs. Only M019R.X1 showed a complete duplication of chromosome 7. **C.** Validation of the absence of the *BRAF* amplification was performed by qPCR on genomic. *CRAF* was included as a negative control. CT values were normalized to *LINE*. Error bars indicate standard deviation.

Figure S4. Validation of the mechanisms and the resistance in PDX, Related to Figure 2 and 3.
A. Validation of $NRAS^{Q61K}$ ($NRAS^{C181A}$) mutation in M026R.X1 and **B.** M029R.X1 by Sanger sequencing. **C.** Validation of $AKT3^{L51R}$ ($AKT3^{T152G}$) mutation in M048R2.X1 by Sanger sequencing. **D.** Staining for p-ERK on FFPE material of the matched PDX pairs M026/R.X2, M029/R.X2 and M009/R.X2 treated with vehicle or 30 mg/kg dabrafenib. Scale bars indicate 100 μm.

Figure S5. Analysis of a panel of pre-treatment PDX for presence of $BRAF^{V600E/DK}$, Related to Figure 5.
Immunoblotting to detect the presence of $BRAF^{V600E/DK}$ in a panel of pre-treatment PDX, using two different antibodies, recognizing either a N-terminal epitope ($BRAF^{NT}$) or the $BRAF^{V600E}$ epitope. Vinculin was used as a loading control.

Figure S6. Visualization of structural variants and DNA copy number aberrations, Related to Figure 6.
A. The two genomic breakpoints in A375R that resulted in the establishment of a gene encoding $BRAF^{V600E/DK}$. **B.** The two genomic breakpoints in 888melDR that resulted in the establishment of a gene encoding $BRAF^{V600E/DK}$. Red arrows indicate the location of the breaks, the blue star indicates the genomic location where the breakpoint is located after the duplication of the BRAF kinase domain. **C.** Circos plots visualizing the structural variants **(**SV) and DNA copy number aberrations detected in parental cell line 888mel and double resistant cell line 888melDR. Blue indicates inter-chromosomal SVs, red intra-chromosomal SV. **D.** Circos plots visualizing the SV and DNA copy number aberrations detected in 888melDR but not in 888mel, both genome wide (top) and for the three chromosomes associated with the amplification on chromosome 7 which includes *BRAF* (bottom). **E.** Circos plot visualising the SVs and DNA copy number aberrations detected in resistant cell lines A375R. **F.** Read count data for A375R for the *BRAF* locus. Each dot represents the average number (log_2) of reads per 5kb.

Figure S7. Mass Spectrometry Identification of $BRAF^{V600E/DK}$ protein, Related to Figure 6.
A. SDS-PAGE showing the result of the IP on the parental cell line 888mel and resistant cell line 888melDR. Blot shows input before IP (input), result after IP (IP) and left-over in the buffer (after IP)

B. Tryptic digest of the suspected $BRAF^{V600E/DK}$ gel band was analysed by LC-MS/MS. Sequence coverage of the predicted protein sequence was around 50%, with the protein sequence covered by identified peptides indicated in green. **C.** The covered sequence included the unique $BRAF^{V600E/DK}$ fusion peptide, unambiguously demonstrating duplication of the BRAF kinase domain and confirming the protein sequence predicted by the RNA-sequencing data.

Table S1. Success rate PDX platform, Related to Figure 1

Tumor samples	Number	Xenografted	Cell lines derived of PDX
$BRAF^{V600E/K}$	86	73 (85%)	21 (29%)
$NRAS^{Q61}$	10	10 (100%)	3 (30%)
$BRAF^{WT}NRAS^{WT}$	7	6 (85%)	3 (50%)
Total	103	89 (86%)	27 (30%)
Whole exome sequencing		19	
360-cancer gene panel		47	

Table S2. Tumor percentage of matched PDX pairs, Related to Figure 2

PDX	Tumor cells (%)	Tumor stroma (%)	Necrosis/ degeneration/ hemorrhage (%)
M005.X1	70	25	5
M005R.X1	60	35	5
M009.X1	99	1	0
M009R.X1	87	3	10
M019.X1	80	5	15
M019R.X1	95	5	0
M026.X1	40	1	59
M026R.X1	15	1	84
M029.X1	98	1	1
M029R.X1	84	1	15
M048.X1	90	10	0
M048R1.X1	90	5	5
M048R2.X1	80	3	17

Table S3. Mutations detected in PDX panel after targeted sequencing, Related to Figure 4
This table is available as an excel file separately uploaded with this submission.

Table S4. Unmatched PDX samples, Related to Figure 5

Tumor samples	Pre-treatment	Post-treatment	Total
$BRAF^{V600E}$	19	19	38
$NRAS^{Q61}$	2	1	3
$BRAF^{WT}NRAS^{WT}$	2		2
TIL therapy		5	5
Total			47

Table S5. Previously known resistance mechanisms present in PDX derived from vemurafenib-resistant patients, Related to Figure 5

Sample	Best Clinical response	Duration	Resistance mechanism	Reference
M001R.X1	PR	10 months	$BRAF^{L505H}$	(Choi et al., 2014; Wagenaar et al., 2014)
M004R.X1	PR	4 months	BRAF splicing	(Poulikakos et al., 2011)
M006R.X1	PR	4 months	$NRAS^{Q61K}$ BRAF splicing	(Nazarian et al., 2010; Poulikakos et al., 2011)
M010R.X1	SD	6 months	MITF amplification	(Van Allen et al., 2014)
M013R.X1	PR	6 months	$PIK3CA^{E545K}$ Loss of PTEN	(Paraiso et al., 2011; Shi et al., 2014)
M014R.X1	PR	12 months		
M031R.X1	PR	7 months	BRAF splicing	(Poulikakos et al., 2011)
M033R.X1	CR	6 months		
M034R.X1	PR	10 months		
M039R.X1	PR	10 months	BRAF splicing Loss of PTEN	(Paraiso et al., 2011; Poulikakos et al., 2011)
M042R.X1	PR	8 months	BRAF amplification	(Thakur et al., 2013)
M044R.X1	SD	10 months	MET overexpression	(Vergani et al., 2011)
M054R.X1	SD	12 months		
M056R.X1	MR	6 months	$MAP2K1^{E203K}$ BRAF splicing EGFR overexpression	(Nikolaev et al., 2012; Poulikakos et al., 2011; Prahallad et al., 2012)
M060R.X1	PR	10 months	$PIK3CA^{E545K}$ EGFR overexpression	(Prahallad et al., 2012; Shi et al., 2014)
M061R.X1	PR	10 months	EGFR overexpression	(Prahallad et al., 2012)
M062R.X1	PR	12 months	$BRAF^{L505H}$ MITF amplification	(Choi et al., 2014; Van Allen et al., 2014; Wagenaar et al., 2014)
M063R.X1	SD	4 months		
M074R.X1	PD	2 months		

PR = partial response, SD = stable disease, CR = complete response, MR = mixed response

Table S6. Sample identifiers and number of supporting reads from RNAseq for BRAF$^{V600E/DK}$ detected in an independent dataset, Related to Figure 6.

GEO ID	Patient ID	Treatment	# reads
GSM1588858	Pt3-DP1	BRAFi	2
GSM1588860	Pt3-DP3	BRAFi	7
GSM1588901	Pt20-DDP1	BRAFi+MEKi	45
GSM1588902	Pt20-DP1	BRAFi	12

Table S7. Primers and hairpins, Related to Figure 2, 6 and 7.

Primer name	Sequence
$NRAS^{Q61K}$-F	5'- GATTCTTACAGAAAACAAGTG-3'
$NRAS^{Q61K}$-R	5'- ATGACTTGCTATTATTGATGG-3'
$AKT3^{L51R}$-F	5'- TGGAGGCCAAGATACTTCCTT-3'
$AKT3^{L51R}$-R	5'- ATGTGTTTGGCTTTGGTCGT-3'
$AKT3^{L51R}$-seq	5'- GGCTCATTCATAGGATATAA-3'
LINE-F	5'- AAAGCCGCTCAACTACATGG-3'
LINE-R	5'- TGCTTTGAATGCGTCCCAGAG-3'
CRAF-F	5'- CAACTGATTGCACTGACTGCCAAC-3'
CRAF-R	5'- CCAGCTTTCTACTCACCGCACAAC-3'
BRAF-F	5'- CAAGTCACCACAAAAACCTATCGT-3'
BRAF-R	5'- AACTGACTCACCACTGTCCTCTGTT-3'
BRAF-exon 18-F	5'-ATTCTCGCCTCTATTGAGCT-3'
BRAF-exon 10-R	5'- AAGGCTTTCACGTTAGTTAG-3'
BRAF-exon 9-F	5'-AGACCAAGGATTTCGTGGTGA-3'
BRAF-exon 10-R	5'- AGTGAGCCAGGTAATGAGGCA-3'
$BRAF^{V600E/DK}$-breakpoint-A375R-F	5'-GCCAGGCTCAAAATCAAACA-3'
$BRAF^{V600E/DK}$-breakpoint-A375R-R	5'-TGCACAGGCATTCATAGAAA-3'
$BRAF^{V600E/DK}$-breakpoint-888melDR-F	5'-TTTTTTTTTGAGATGGAGCTTGCTC-3'
$BRAF^{V600E/DK}$-breakpoint-888melDR-R	5'-GACTAAGTAATTGAAACAAAAG-3'
$BRAF^{V600E/DK}$-F-XbaI	5'- GGGTCTAGAATGGCCGGCTCTCGGTTATAAGATG-3'
$BRAF^{V600E/DK}$-R-SwaI	5'-GGGATTTAAATTCAGTGGACAGGAAACGCACCAT-3'
$BRAF^{V600E/DK}$ shRNA#1-F:	5'-CCGGgatatggatcaaccacaggtCTCGAGacctgtggttgatccatatccTTTTTG-3'
$BRAF^{V600E/DK}$ shRNA#1-R	5'-AATTCAAAAAggatatggatcaaccacaggtCTCGAGacctgtggttgatccatatcc-3'
$BRAF^{V600E/DK}$ shRNA#2-F	5'-CCGGtatggatcaaccacaggtttgCTCGAGcaaacctgtggttgatccataTTTTTG-3'
$BRAF^{V600E/DK}$ shRNA#2-R	5'-AATTCAAAAAtatggatcaaccacaggtttgCTCGAGcaaacctgtggttgatccata-3'

Supplemental Experimental Procedures

Response data patients
CT scans were used to determine the size of independent lesions at different time points. The size of a lesion was defined as the longest in plane diameter (in mm), measured manually by the tool provided in the Inter PACS Viewing & sharing System. For consistency, every lesion was measured by the same person on all subsequent CT scans. To ensure objectivity, this person was blinded for any other data of the patient in question.

DNA isolation
DNA was isolated from granulocytes derived from peripheral blood and tumor fragments using the DNA Easy Blood & Tissue Kit (Qiagen) according to manufacturer's protocol. DNA content was measured using Picogreen (P7581) according to manufacturer's protocol.

ArrayCGH analysis
DNA samples and normal genomic DNA (female, G1521, Promega) were labeled with CGH labeling kit for BAC Arrays (Enzo Life Sciences) according to manufacturer's protocol. After labeling, the samples were hybridized on a Nimblegen array (090527_HG18_WG_CGH_v3.1_HX12,_GEO platform ID: GPL17641). Image acquisition of the Nimblegen arrays was performed using the Agilent DNA Microarray Scanner (Model G2505B, Serial number US22502518) and image analysis was performed using Nimblescan software version 2.6 (Roche Nimblegen). Segmentation of all copy number profiles was calculated using circular binary segmentation (CBS) as implemented in the R-package CGHcall 2.22.0 (van de Wiel et al., 2011).

Whole Genome Sequencing of cell lines
DNA of parental 888mel, dabrafenib and trametinib double resistant 888mel (888melDR) and PLX4720-resistant A375 (A375R) was isolated as described above. Sequencing with 151bp paired-end reads of sequence libraries was performed on the Illumina X10 analyzer. Reads were mapped to the Sanger human reference (hg19) and BAM files were binary compressed, sorted and indexed by SAMtools (samtools view, sort and index tools), duplicated reads were removed by Picard (with MarkDuplicates) and base quality score recalibration and local realignment around indels followed the recommended workflow of the GATK toolkit (RealignerTargetCreator, IndelRealigner, BaseRecalibrator and PrintReads). Sequencing data has been made available through the European Genome-phenome Archive (EGA; http://www.ebi.ac.uk/ega/home; accession number EGAS00001001304).

Whole exome sequencing of matched PDX
DNA of 21 PDX samples with matching reference (blood) was isolated as described above and subjected to whole exome sequencing. Exome enrichment was performed using the Agilent SureSelect Human Exon Kit 50Mb capture set (Agilent, G3362). Sequencing with 75bp paired-end reads of targeted-enrichment libraries was performed on an Illumina HiSeq 2000 analyzer. Reads were mapped by bwa 0-7.5 with default settings to the human reference (hg19) and mouse reference (mm10), the latter for later removal of reads from mouse origin, as described below. BAM files were processed using Picard [1.101], SAMtools [0.1.18] and the Genome Analysis ToolKit (GATK) release 2.7-4. BAM files were binary compressed, sorted and indexed by SAMtools (samtools view, sort and index tools), duplicated reads were removed by Picard (with MarkDuplicates) and base quality score recalibration and local realignment around indels followed the recommended workflow of the GATK toolkit (RealignerTargetCreator, IndelRealigner, BaseRecalibrator and PrintReads). BAM files were further processed by removing reads that originate from mouse with XenofilteR release version 1.3 (https://github.com/PeeperLab/XenofilteR, Kluin and Krijgsman, manuscript in preparation. For each read-pair we summed the number of soft-clips, mismatches and inserts, both for mapping against the human as well as the mouse reference. The derived scores were used to classify reads as either mouse or human. Only reads with a lower score in human compared to mapping to mouse were retained in the final bam files.

Variants were called by GATK 2.7-4 using the 'UnifiedGenotyper' with default settings except for "-minIndelFrac" which was set to 10%. Annotation of the vcf files was performed with ANNOVAR (release 2014, October) (http://www.openbioinformatics.org/annovar/). All variants detected in the germ-line (blood) samples with a Variant Allele Frequency (VAF) over 5% were excluded from further analysis. Variants were further filtered: minimum VAF of 5% in at least one of the samples; a

minimum of 10x coverage in a least one of the samples; variant positions must not be listed as a single nucleotide polymorphism (SNP) in the 1000 Genome project except when present in COSMIC; Variant position must be annotated as exonic by RefSeq (Release 45); synonymous/non-synonymous calls were made and the synonymous excluded from further analysis. All filtering was performed with R 3.1.1 using in-house parsers. Sequencing data has been made available through the European Genome-phenome Archive (EGA; http://www.ebi.ac.uk/ega/home; accession number EGAS00001000415 and EGAS00001000617).

Targeted sequencing of unmatched PDX

DNA of 48 PDX samples was isolated as described above and subjected to targeted sequencing of 360 established and putative cancer-related genes using custom-made bait set (Agilent Technologies) for target enrichment. Paired-end sequencing was performed on Illumina HiSeq 2000 or 2500 analyzers. The raw sequence reads were processed similar to the WES data with the difference that no blood reference was available. The observed variants were referenced with polymorphisms catalogued by the 1000 genomes project (1000 Genomes Project Consortium et al., 2010) to remove known germline variants. Sequencing data has been made available through the European Genome-phenome Archive (EGA; http://www.ebi.ac.uk/ega/home; dataset ID: study ID: EGAS00001000655)

DNA copy number profiles

BAM files from targeted sequencing and whole exome sequencing were analyzed for DNA copy number aberrations by CopywriteR (Kuilman et al., 2015). DNA copy number profiles of matched PDX samples, analyzed with whole exome sequencing, were generated with 20kb bins, resulting in ~137K data points evenly distributed over the genome. Log_2ratios were calculated for tumor samples versus reference (blood) sample.

DNA copy number profiles of unmatched PDX samples, analyzed with targeted sequencing, were generated with 100kb bins, resulting in ~25K data points evenly distributed over the genome. Log_2 values were calculated based on tumor samples without a reference as described in (Kuilman et al., 2015).

DNA copy number profiles of cell lines 888mel, 888melDR and A375R, analyzed with WGS, were generated with 5kb bins evenly distributed over the genome. The resulting read count data was normalized similar to the WES data by loess normalization based on GC-content and mappability. Differences in DNA copy number between parental 888mel and 888melDR were assessed by subtracting the log2 of the read count of 888mel from the log2 read count of 888melDR. All normalized profiles were further analyzed by circular binary segmentation (CBS) (Venkatraman and Olshen, 2007).

Structural variation in WGS

Structural variations in cell lines 888mel, 888melDR and A375R were assessed directly on the WGS bam files with breakdancer (Chen et al., 2009). Only structural variants with a confidence score of 99 and a minimum of 10 supporting reads were used for the analysis. In addition, the minimum length between 2 intra-chromosomal breakpoints was set to 1mb. To assess the difference between 888mel and 888melDR all structural variants present in 888mel were removed from the list of structural variations in 888melDR. Circos plots were generated with (Zhang et al., 2015) using the DNA copy number data as described above and the filtered list of structural variations.

RNA isolation and sequencing

RNA isolated by Trizol, according to manufacturers protocol, from Fresh-Frozen (FF) PDX samples and Formalin-Fixed, Paraffin-Embedded (FFPE) patient archival tissue was sequenced with 50bp single-end sequencing on an Illumina HiSeq2000. Read counts per gene were quantified using HTSeq version 0.5.4. Read mapping was performed using TopHat version 2.0.9 with the NCBI Build 37 reference genome. Read counts were transformed by applying a variance stabilization with DESeq (1.12.1). In DESeq the dispersion estimate estimateDispersions had parameters: *method* 'per-condition' and *fitType* 'local' and for null model evaluation with no replicates *method* 'blind', and *sharingMode* 'fit-only'. Gene expression differences between PDX (FF) and patient (FFPE) read count data were observed by cluster analysis. Of the 21.467 genes in the initial analysis 1399 genes were differentially expressed (FDR<0.2) between the PDX and patient samples. After removal of these 1,399 genes the samples were clustered again with the remaining 20,068 genes. Heatmaps were generated with gplots

(2.12.1) as available through Bioconductor. Analysis was performed, and plots were made using the statistical programming language R (v 3.0.2).

RNA isolated from 4 FF PDX samples (M010R.X1, M033R.X1, M063R.X1 and M048R2.X1) was sequenced with 65bp paired-end sequencing on an Illumina HiSeq 2500. Discordant read pairs with both reads mapping within in BRAF were identified from the Tophat 'fusions.out' file and visually inspected in IGV to verify the breakpoints associated with the $BRAF^{V600E}$ kinase duplication. Both RNA sequence data sets are available through accession number GSE73738.

Raw data (fastq) from an independent dataset (Hugo et al., 2015) were downloaded from NCBI's Sequence Read Archive (SRA, SRP052740). Read mapping was performed using TopHat version 2.0.9 with the NCBI Build 38 reference genome. Discordant read pairs with both reads mapping within in BRAF were identified from the Tophat 'fusions.out' file and visually inspected in IGV to verify the breakpoints associated with the $BRAF^{V600E}$ kinase duplication.

FISH

Preparation of metaphase chromosome spread from parental Mel888 and double resistance Mel888 was performed as previously described (van Steensel et al., 1998).Two-color metaphase FISH was performed using chromosome 7 centromere probe (Chr7 CEP GR, G100527G-8, Agilent) and BRAF probe (7q34 BRAF-CN RD, G100368R-8, Agilent) according to the manufacturer's protocol.

Mass-spectrometry analysis of $BRAF^{V600E/DK}$

Mouse-anti-B-RAF (F7, Santa Cruz) antibodies were cross-linked to Dynabeads protein G (Cat #:10003D) according to the manufacturer's instruction. Cell lysates were incubated with these Dynabeads for 2h at 4°C. After washing 5 times with immunoprecipitation (IP) buffer (50 mM Tris-Cl, pH 8.0, 150 mM NaCl, 1.0% NP-40), elution was performed by boiling in NaPAGE LDS sample buffer (NP0008, Novex) and then processed for SDS-PAGE. Following staining of the SDS-PAGE gel with GelCode Blue stain (Pierce), the $BRAF^{V600E/DK}$ protein band was excised, proteins in the gel plug were reduced with DTT (1 hr at 60^0C) and subsequently alkylated using iodoacetamide (30 min at RT in the dark). In-gel digestion with 3ng/uL trypsin (Gold, Mass Spectrometry Grade, Promega) in 50 mM ammonium bicarbonate (pH 8.5) was performed overnight at 37 ^{o}C. After digestion, peptides were extracted with acetonitrile and dried down in a speed vacuum centrifuge. Prior to mass spectrometry analysis, the peptides were reconstituted in 10% formic acid.

Peptides were separated using the Proxeon nLC 1000 system (Thermo Scientific, Bremen) fitted with a trapping (ReproSil-Pur 120 C18-AQ 3µm (Dr. Maisch GmbH, Ammerbuch, Germany); 100 µm x 30 mm) and an analytical column (ReproSil-Pur 120 C18-AQ 2.4 µm (Dr. Maisch GmbH); 75 µm x 500 mm), both packed in-house. The outlet of the analytical column was coupled directly to a Thermo Orbitrap Fusion hybrid mass spectrometer (Q-OT-qIT, Thermo Scientific) using the Proxeon nanoflex source. Nanospray was achieved using a distally coated fused silica tip emitter (generated in-house, o.d. 375 µm, i.d. 20 µm) operated at 2.1 kV. Solvent A was 0.1% formic acid/water and solvent B was 0.1% formic acid/ACN. An aliquot (25%) of the in-gel digest was eluted from the analytical column at a constant flow rate of 250 nl/min in a 35-min gradient, containing a linear increase from 7% to 25% solvent B, followed by wash at 80% solvent B. Survey scans of peptide precursors from m/z 375-1500 were performed at 120K resolution with a 4 x 10^5 ion count target. Tandem MS was performed by quadrupole isolation at 1.6 Th, followed by HCD fragmentation with normalized collision energy of 33 and ion trap MS^2 fragment detection. The MS^2 ion count target was set to 10^4 and the max injection time was set to 50 ms. Only precursors with charge state 2-6 were sampled for MS^2. Monoisotopic precursor selection was turned on; the dynamic exclusion duration was set to 30s with a 10 ppm tolerance around the selected precursor and its isotopes. The instrument was run in top speed mode with 3 s cycles.

Raw data files were processed using Proteome Discoverer (version 1.4.1.14, Thermo Fisher Scientific). MS^2 spectra were searched against a custom database containing contaminants and the predicted sequence of the $BRAF^{V600E/DK}$ protein using Mascot (version 2.4.1, Matrix Science, UK). Carbamidomethylation of cysteines was set as fixed modification and oxidation of methionine was set as a variable modification. Trypsin was specified as enzyme and up to two miscleavages were allowed. Data filtering was performed using percolator, resulting in 1% false discovery rate (FDR), and peptide ion score >20.

Supplemental References

1000 Genomes Project Consortium, Abecasis, G.R., Altshuler, D., Auton, A., Brooks, L.D., Durbin, R.M., Gibbs, R.A., Hurles, M.E., and McVean, G.A. (2010). A map of human genome variation from population-scale sequencing. Nature *467*, 1061–1073.

Chen, K., Wallis, J.W., McLellan, M.D., Larson, D.E., Kalicki, J.M., Pohl, C.S., McGrath, S.D., Wendl, M.C., Zhang, Q., Locke, D.P., et al. (2009). BreakDancer: an algorithm for high-resolution mapping of genomic structural variation. Nat Meth *6*, 677–681.

Choi, J., Landrette, S.F., Wang, T., Evans, P., Bacchiocchi, A., Bjornson, R., Cheng, E., Stiegler, A.L., Gathiaka, S., Acevedo, O., et al. (2014). Identification of PLX4032-resistance mechanisms and implications for novel RAF inhibitors. Pigment Cell & Melanoma Research *27*, 253–262.

Hugo, W., Shi, H., Sun, L., Piva, M., Song, C., Kong, X., Moriceau, G., Hong, A., Dahlman, K.B., Johnson, D.B., et al. (2015). Non-genomic and Immune Evolution of Melanoma Acquiring MAPKi Resistance. Cell *162*, 1271–1285.

Kuilman, T., Velds, A., Kemper, K., Ranzani, M., Bombardelli, L., Hoogstraat, M., Nevedomskaya, E., Xu, G., de Ruiter, J., Lolkema, M.P., et al. (2015). CopywriteR: DNA copy number detection from off-target sequence data. Genome Biology *16*, R163.

Nazarian, R., Shi, H., Wang, Q., Kong, X., Koya, R.C., Lee, H., Chen, Z., Lee, M.-K., Attar, N., Sazegar, H., et al. (2010). Melanomas acquire resistance to B-RAF(V600E) inhibition by RTK or N-RAS upregulation. Nature *468*, 973–977.

Nikolaev, S.I., Rimoldi, D., Iseli, C., Valsesia, A., Robyr, D., Gehrig, C., Harshman, K., Guipponi, M., Bukach, O., Zoete, V., et al. (2012). Exome sequencing identifies recurrent somatic MAP2K1 and MAP2K2 mutations in melanoma. Nature Genetics *44*, 133–139.

Paraiso, K.H.T., Xiang, Y., Rebecca, V.W., Abel, E.V., Chen, Y.A., Munko, A.C., Wood, E., Fedorenko, I.V., Sondak, V.K., Anderson, A.R.A., et al. (2011). PTEN loss confers BRAF inhibitor resistance to melanoma cells through the suppression of BIM expression. Cancer Res. *71*, 2750–2760.

Possik, P.A., Müller, J., Gerlach, C., Kenski, J.C.N., Huang, X., Shahrabi, A., Krijgsman, O., Song, J.-Y., Smit, M.A., Gerritsen, B., et al. (2014). Parallel in vivo and in vitro melanoma RNAi dropout screens reveal synthetic lethality between hypoxia and DNA damage response inhibition. Cell Rep *9*, 1375–1386.

Poulikakos, P.I., Persaud, Y., Janakiraman, M., Kong, X., Ng, C., Moriceau, G., Shi, H., Atefi, M., Titz, B., Gabay, M.T., et al. (2011). RAF inhibitor resistance is mediated by dimerization of aberrantly spliced BRAF(V600E). Nature *480*, 387–390.

Prahallad, A., Sun, C., Huang, S., Di Nicolantonio, F., Salazar, R., Zecchin, D., Beijersbergen, R.L., Bardelli, A., and Bernards, R. (2012). Unresponsiveness of colon cancer to BRAF(V600E) inhibition through feedback activation of EGFR. Nature *483*, 100–103.

Shi, H., Hong, A., Kong, X., Koya, R.C., Song, C., Moriceau, G., Hugo, W., Yu, C.C., Ng, C., Chodon, T., et al. (2014). A novel AKT1 mutant amplifies an adaptive melanoma response to BRAF inhibition. Cancer Discovery *4*, 69–79.

Thakur, Das, M., Salangsang, F., Landman, A.S., Sellers, W.R., Pryer, N.K., Levesque, M.P., Dummer, R., McMahon, M., and Stuart, D.D. (2013). Modelling vemurafenib resistance in melanoma reveals a strategy to forestall drug resistance. Nature *494*, 251–255.

Van Allen, E.M., Wagle, N., Sucker, A., Treacy, D.J., Johannessen, C.M., Goetz, E.M., Place, C.S., Taylor-Weiner, A., Whittaker, S., Kryukov, G.V., et al. (2014). The genetic landscape of clinical resistance to RAF inhibition in metastatic melanoma. Cancer Discovery *4*, 94–109.

van de Wiel, M.A., Picard, F., van Wieringen, W.N., and Ylstra, B. (2011). Preprocessing and

downstream analysis of microarray DNA copy number profiles. Brief. Bioinformatics *12*, 10–21.

van Steensel, B., Smogorzewska, A., and de Lange, T. (1998). TRF2 protects human telomeres from end-to-end fusions. Cell *92*, 401–413.

Venkatraman, E.S., and Olshen, A.B. (2007). A faster circular binary segmentation algorithm for the analysis of array CGH data. Bioinformatics *23*, 657–663.

Vergani, E., Vallacchi, V., Frigerio, S., Deho, P., Mondellini, P., Perego, P., Cassinelli, G., Lanzi, C., Testi, M.A., Rivoltini, L., et al. (2011). Identification of MET and SRC activation in melanoma cell lines showing primary resistance to PLX4032. Neoplasia *13*, 1132–1142.

Vredeveld, L.C.W., Possik, P.A., Smit, M.A., Meissl, K., Michaloglou, C., Horlings, H.M., Ajouaou, A., Kortman, P.C., Dankort, D., McMahon, M., et al. (2012). Abrogation of BRAFV600E-induced senescence by PI3K pathway activation contributes to melanomagenesis. Genes & Development *26*, 1055–1069.

Wagenaar, T.R., Ma, L., Roscoe, B., Park, S.M., Bolon, D.N., and Green, M.R. (2014). Resistance to vemurafenib resulting from a novel mutation in the BRAFV600E kinase domain. Pigment Cell & Melanoma Research *27*, 124–133.

Zhang, L., Zhou, Y., Cheng, C., Cui, H., Cheng, L., Kong, P., Wang, J., Li, Y., Chen, W., Song, B., et al. (2015). Genomic analyses reveal mutational signatures and frequently altered genes in esophageal squamous cell carcinoma. Am. J. Hum. Genet. *96*, 597–611.